

## The mechanochemical origins of the microtubule sliding motility within the kinesin-5 domain organization

Stanley Nithianantham\*, Malina K. Iwanski\*<sup>2</sup>, Ignas Gaska\*, Himanshu Pandey, Tatyana Bodrug, Sayaka Inagaki<sup>4</sup>, Jennifer Major<sup>4</sup>, Gary J. Brouhard<sup>2</sup>, Larissa Gheber, Steven S. Rosenfeld<sup>4</sup>, Scott Forth<sup>ψ</sup>, Adam G. Hendricks<sup>ψ2</sup>, Jawdat Al-Bassam<sup>ψ</sup>

<sup>1</sup> Dept. of Molecular and Cellular Biology, University of California, Davis, CA

<sup>2</sup> Dept. of Biology, Dept. of Bioengineering, McGill University, Montreal, QC

<sup>3</sup> Dept. of Biology, Rensselaer Polytechnic Institute, Troy

<sup>3</sup> Dept. of Chemistry, The Ben Gurion University, Ber Sheva, Israel

<sup>4</sup> Dept. of Pharmacology, Mayo Clinic, Jacksonville, FL

\* These authors contributed equally to this work

<sup>ψ</sup> These authors are co-corresponding

### Abstract

The conserved kinesin-5 bipolar tetrameric motors slide apart microtubules during mitotic spindle assembly and elongation. Kinesin-5 bipolar organization originates from its conserved tetrameric helical minifilament, which position the C-terminal tail domains of two subunits near the N-terminal motor domains of two anti-parallel subunits (Scholey et al, 2014). This unique tetrameric structure enables kinesin-5 to simultaneously engage two microtubules and transmit forces between them, and for multiple kinesin-5 motors to organize via tail to motor interactions during microtubule sliding (Bodrug et al, 2020). Here, we show how these two structural adaptations, the kinesin-5 tail-motor domain interactions and the length of the tetrameric minifilament, determine critical aspects of kinesin-5 motility and sliding mechanisms. An x-ray structure of the 34-nm kinesin-5 minifilament reveals how the dual dimeric N-terminal coiled-coils emerge from the tetrameric central bundle. Using this structure, we generated active bipolar mini-tetrameric motors from *Drosophila* and human orthologs, which are half the length of native kinesin-5. Using single-molecule motility assays, we show that kinesin-5 tail domains promote mini-tetramers static pauses that punctuate processive motility. During such pauses, kinesin-5 mini-tetramers form multi-motor clusters mediated via tail to motor domain cross-interactions. These clusters undergo slow and highly processive motility and accumulate at microtubule plus-ends. In contrast to native kinesin-5, mini-tetramers require tail domains to initiate microtubule crosslinking. Although mini-tetramers are highly strained in initially aligning microtubules, they slide microtubules more efficiently than native kinesin-5, due to their decreased minifilament flexibility. Our studies reveal that the conserved kinesin-5 motor-tail mediated clustering and the length of the tetrameric minifilament are key features for sliding motility and are critical in organizing microtubules during mitotic spindle assembly and elongation.

### Introduction

During cell division, microtubules (MTs) are rearranged into bipolar mitotic spindles from two overlapping MT asters during metaphase. Kinesin-5 motors are conserved across eukaryotes and are essential for the assembly and elongation of bipolar mitotic spindles. Kinesin-5 motors are 60-80 nm bipolar tetrameric proteins with a pair of N-terminal motor and C-terminal tail domains on either end of an  $\alpha$ -helical central tetrameric minifilament (Kashina et al., 1996; Scholey et al., 2014). Although kinesin-5 motors are conserved across eukaryotes, there is a remarkable diversity in their mechanisms across species with the yeast kinesin-5 motors uniquely undergoing minus end directed motility as single motors, and switching direction upon clustering or during MT sliding toward plus-end directed motility (Pandey et al., 2021a; Pandey

53 et al., 2021b; Shapira et al., 2017; Singh et al., 2018). In contrast, metazoan Kinesin-5 motors  
54 undergo motility towards MT plus ends both along single MTs and when sliding MTs (Bodrug et  
55 al., 2020; Kapitein et al., 2005; Weinger et al., 2011).

56  
57 Kinesin-5 motors slide apart MTs emanating from opposing spindle poles at the midzone region  
58 by initially crosslinking, then aligning these MTs by undergoing motility with their bipolar ends  
59 along two MTs using their unique tetrameric architecture (Kashina et al., 1996). This kinesin-5  
60 MT sliding activity is conserved and critical for organizing bipolar mitotic spindles. The kinesin-5  
61 tetrameric bipolar organization originates from the anti-parallel folding of the four  $\alpha$ -helices from  
62 the four subunits within the Bipolar assembly (BASS) domain (Scholey et al., 2014). The BASS  
63 domain lies at the center of the kinesin-5 minifilament and forms the central force-bearing  
64 structure that coordinates between the two motile motor ends, each of which supports hand  
65 over-hand motility along MTs. While the kinesin-5 MT sliding motility is linked to the motor's  
66 bipolar tetrameric organization, the functional relationship between the conserved kinesin-5  
67 motor, tail or BASS domains and the unique MT crosslinking or MT sliding mechanisms remains  
68 unknown (Kapitein et al., 2005).

69  
70 The kinesin-5 C-terminal tail domains (termed tail from herein) emerge from bipolar tetrameric  
71 minifilament near the motor domains of the antiparallel dimeric folded subunits (Acar et al.,  
72 2013) and kinesin-5 tails are essential for MT sliding activity across species (Duselder et al.,  
73 2015; Hildebrandt et al., 2006; Weinger et al., 2011). We recently discovered that the kinesin-5  
74 tail regulates the MT-activated ATP hydrolysis in the motor domains and this regulation is  
75 essential for kinesin-5 motors to transition from crosslinking to MT sliding motility (Bodrug et al.,  
76 2020). This allosteric tail to motor domain interaction allow for trans interactions between  
77 multiple kinesin-5 motors, resulting in multi-motor clustering (Bodrug et al., 2020). Tail-mediated  
78 clustering is a critical for organizing the forces generated by multiple kinesin-5 motors promote  
79 the alignment of MTs to crosslinked paired MTs then modulate their sliding (Bodrug et al., 2020).  
80 However, it remains unknown how this tail- to motor regulation is impacted by the distinct  
81 kinesin-5 central minifilament organization and how these two features regulate MT crosslinking,  
82 alignment and sliding.

83  
84 Here, we describe how the kinesin-5 tail-motor domain interaction and the length of the  
85 tetrameric minifilament modulate kinesin-5 motor clustering, MT crosslinking, and MT sliding  
86 activities. We determined an x-ray structure of a 34-nm extended BASS  $\alpha$ -helical tetramer,  
87 revealing rigid dimeric parallel N-terminal coiled-coil junctions that emerge from its central  
88 tetrameric core. Using this structure as a platform, we engineered short human and *Drosophila*  
89 bipolar 38-nm mini-tetrameric kinesin-5 motors, which are roughly half the length of native  
90 kinesin-5 motors. Single-molecule motility assays reveal mini-tetramers without tail domains  
91 undergo processive motility with infrequent pauses in which motors statically bind MTs without  
92 diffusing. The tail domains enhance kinesin-5 mini-tetramer pausing and promote the assembly  
93 of multiple motors into clusters. These multi-motor clusters assemble when motile motors  
94 encounter paused motors along the MT. MT sliding assays reveal that unlike the native kinesin-5  
95 motor, kinesin-5 mini-tetramers require the tail domain to crosslink, align and slide two MTs.  
96 Kinesin-5 mini-tetramers are restricted in their ability to pair and align MTs. However, once MTs  
97 are paired, these mini-tetramers slide these MTs more efficiently than native kinesin-5. Our data  
98 demonstrate that the kinesin-5 tail and length of the minifilament are two critical structural  
99 adaptations that allow it to effectively crosslink and slide apart MTs. The tail domain is required  
100 to mediate motor pausing and clustering such that multiple motors can coordinate in MT  
101 overlaps. The length of the kinesin-5 minifilament is critical to provide flexibility required for  
102 efficient MT crosslinking and transmission of forces during MT alignment and sliding.

103  
104 **Results**

105  
106  
107  
108  
109  
110  
111  
112  
113  
114  
115  
116  
117  
118  
119  
120  
121  
122  
123  
124  
125  
126  
127  
128  
129  
130  
131  
132  
133  
134  
135  
136  
137  
138  
139  
140  
141  
142  
143  
144  
145  
146  
147  
148  
149  
150  
151  
152  
153  
154  
155  
156

## **An extended BASS x-ray structure reveals rigid and dimeric coiled-coils emerging from bipolar tetramer junctions**

To determine the organization of bipolar kinesin-5 minifilament and how the dimeric  $\alpha$ -helical coiled-coil junctions are formed, we solved the x-ray structure of an extended *Drosophila melanogaster* KLP61F segment (residues 620-804) in which the kinesin-5 sequence is extended by 40 residues N-terminally compared to the previous BASS x-ray structure (Scholey et al 2014; termed BASS-XL from herein). The KLP61F BASS-XL was purified and crystallized in the space group C2 (253.18-Å, 84.89-Å, 96.77-Å) (Figure 1 figure supplement 1). The X-ray diffraction data were highly anisotropic, indicating translational pseudo-symmetry, and were thus elliptically truncated to 4.4-Å resolution in reciprocal space axes (Figure 1 figure supplement 1; Table 1). The BASS-XL structure was determined by molecular replacement using BASS structure as a starting model and was refined to 4.4-Å resolution leading to a  $R_{\text{work}}/R_{\text{free}}$  (0.277/0.309). The 4.4-Å BASS-XL x-ray crystal structure reveals a 34-nm  $\alpha$ -helical minifilament, compared to the 27-nm BASS minifilament (Figure 1, figure supplement 1A). The structure reveals the N-terminal 30-residues form parallel coiled-coils which emerge from both ends of the BASS tetrameric core (Figure 1A)(Scholey et al., 2014). The N-terminal parallel coiled-coils form multiple heptad repeat interactions with clear a and d contacts forming homotypic interfaces (residues 620-670) (Figure 1B). These dimeric  $\alpha$ -helical coiled-coil extend for 10-nm before they twist slightly out of register into a swap junction (residues 693-697) to form a four  $\alpha$ -helical anti-parallel bundle within the BASS core tetramer (residues 697-760)(Figure 1A)(Scholey et al., 2014). The C-terminus of the BASS-XL forms  $\alpha$ -helices (residues 760-806), which stabilizes a junction of the N-terminal coiled-coil dimer at each end of the BASS tetramer core for the subunit that emerges from the opposite end (Figure 1A). This junction rigidly and tightly orients the BASS-XL N-terminal coiled-coils onto the ends of the BASS core and positions the N-terminal ends of the coiled-coil to be 180° with respect to those emerging from the opposite end of the BASS-XL structure (Figure 1A).

Using the BASS-XL x-ray structure as template for a shortened kinesin-5 minifilament, we engineered bipolar kinesin-5 motors with a 38-nm central minifilament, which we term kinesin-5 mini-tetramers from herein (Figure 1C). Using the pattern of heptad repeats observed in the BASS-XL structure, a longer KLP61F BASS-XL sequence was utilized to generate mini-tetrameric motors by including three coiled-coil heptad repeats (21 residues) on the coiled-coil N-terminus observed in the BASS-XL x-ray structure, leading to a 38-nm long kinesin-5 minifilament (Figure 1 green; 21 residues 597-620). The N-terminal end of this revised 38 nm minifilament was then fused to the C-terminal end of the kinesin-5 motor domain and neck linker (residues 1-365) sequences. On its C-terminus, the BASS-XL mimi-tetramer sequence was either terminated or was C-terminally fused to the N-terminal end of the kinesin-5 tail domain (residues 903-1033) (Figure 1C; Figure 1 figure supplement 2). We generated a structural model for the 38-nm kinesin-5 mini-tetramer, showing its short overall length, which are roughly half the length of the native kinesin-5 (38 nm versus 80 nm)(Acar et al., 2013; Scholey et al., 2014) (Figure 1 figure supplement 2C-D; Figure 1D). The kinesin-5 mini-tetramer model shows that BASS-XL rigidly orients the two dimeric motor domain pairs on both of its ends, positioning them 180° rotated with respect to each other (Figure 1D; Figure 1 figure supplement 2C-D). Using this strategy, we generated two mini-tetrameric constructs from two kinesin-5 orthologs and compared their activities: *Drosophila* KLP61F mini-tetramers (- tail: kMBX, or + tail: kMBXt) or human Eg5 kinesin-5 mini-tetramer motors (-tail: hMBX, or +tail: hMBXt) as described (Figure 1 figure supplement 1A-C; Figure 1C). The motor to coiled-coil junctions for the mini-tetramer constructs are predicted to lack flexibility with the respect to BASS tetrameric core, and to exhibit less torsional flexibility than the full-length native kinesin-5 (Figure 1D). The kinesin-5 mini-tetramer constructs represent only 60% of the full-length kinesin-5 sequence, as they lack 280

157 residues coiled-coil region between the motor neck linker and the extended N-terminal end of  
158 the BASS-XL structure, and 100 residues flexible region between the BASS-XL C-terminal  
159 domain and the N-terminal end of the tail domain (Acar et al., 2013; Bodrug et al., 2020; Scholey  
160 et al., 2014).

161  
162 **Kinesin-5 mini-tetramers undergo processive plus end-directed motility along with**  
163 **pausing.**  
164

165 We reconstituted the motility of kMBX and kMBXt mini-tetramers fused to Neon Green (mNG)  
166 along single MTs imaged them using total internal reflection fluorescence (TIRF) microscopy, as  
167 previously described (Bodrug et al., 2020). Single kMBX mini-tetramer motors undergo slow  
168 processive motility along MTs interspersed very seldom with brief pauses (Figure 2A-B). In  
169 contrast, kMBXt motors undergo processive motility towards MT plus-ends and pause for  
170 extended periods (Figure 2C-D). While paused along MTs, kMBXt motors often encounter other  
171 motile motors and merge to form brighter multi-motor clusters. These clusters of kMBXt motors  
172 undergo motility together as singular entities until reaching MT plus-ends, where they  
173 concentrate for extensive time periods. Thus, kMBXt motors pause for extended periods and  
174 form multi-motor clusters, which are not observed in the case of the kMBX motors, suggesting  
175 that the kinesin-5 tail-motor domain interaction promotes pausing and multi-motor clustering,  
176 recapitulating activities observed for full-length Eg5 (Bodrug et al., 2020).

177  
178 To understand how the *Drosophila* KLP61F tail domain regulates the mini-tetramer motor  
179 properties, we studied how motility of the kMBX and kMBXt are affected by changes in ionic  
180 strength (25, 50, 100 mM KCl). At 25 mM KCl, kMBXt motors undergo very slow motility, which  
181 is 30% slower than kMBX motors (Table 2: 78 vs 115 nm/s). At 50 mM KCl, both kMBX and  
182 kMBXt undergo slightly faster motility, with velocity of kMBX motor being about 10% faster than  
183 kMBXt motors (Table 2: 127 nm/s vs 144 nm/s). At 100 mM KCl, the average motility velocity of  
184 kMBX is 45% higher compared to that for kMBXt motors (Table 2: 156 nm/s vs 114 nm/s). At  
185 higher ionic strengths, kMBXt velocities progressively decreased (Table 2). In contrast, the  
186 kMBX motors bound and dissociated rapidly from MTs at the higher salt concentrations and did  
187 not undergo processive motility. At 25 mM KCl, kMBX motors undergo extremely long run  
188 lengths. At 50 mM KCl, kMBX motors undergo motility at 66% shorter average run lengths than  
189 the kMBXt motors (Table 2: 1014 vs 3135 nm) and 66% shorter run time (Table 2: 9 vs 29 s). At  
190 100 mM KCl, the kMBX motor undergo motility with a 60% shorter average run length compared  
191 to kMBXt (Table 2: 2137 nm vs 5060 nm), and 60% shorter average run time of kMBXt (Table  
192 2: 16 s vs 51 s). These data suggest that the kinesin-5 tail domain down-regulates the motor  
193 domain by decreasing its MT activated ATPase leading to slower motility but increasing run  
194 lengths and run times during each processive motility event.

195  
196 To explore whether the tail-motor interaction and their regulatory mechanism observed for  
197 *Drosophila* KLP61F are conserved in human Eg5, we generated human Eg5 motor mini-  
198 tetramers hMBX (-tail) and hMBXt (+tail) (Figure 2 E-H). The hMBX and hMBXt motors were  
199 engineered with reactive cysteines for labeling with Tetra-methyl Rhodamine (TMR) fluorophores  
200 (see materials and methods). The bright, stable TMR fluorophores on hMBX and hMBXt motors  
201 allowed robust, high-resolution single-molecule tracking analyses. The hMBX motors undergo  
202 processive motility towards MT plus-ends over long distances with infrequent pauses (Figure 2E-  
203 F), while pauses are more frequent for the hMBXt motors containing the tail, similar to our  
204 observation with the kMBXt motors (Figure 2G-H). The hMBXt motors exhibited multiple  
205 intensities with bright and dim spots suggesting multi-motor clustering similar to the properties of  
206 kMBXt motors. Thus, for both *Drosophila* and human kinesin-5 mini-tetramer motors, the  
207 presence of the kinesin-5 C-terminal tail results in slower motors that undergo pauses, form  
208 clusters, and are more processive (Figure 2I, J).

209  
210  
211  
212  
213  
214  
215  
216  
217  
218  
219  
220  
221  
222  
223  
224  
225  
226  
227  
228  
229  
230  
231  
232  
233  
234  
235  
236  
237  
238  
239  
240  
241  
242  
243  
244  
245  
246  
247  
248  
249  
250  
251  
252  
253  
254  
255  
256  
257  
258  
259  
260

## The kinesin-5 tail domain promotes static pausing

To examine kinesin-5 mini-tetramer pausing behavior at the single molecule level, we analyzed the hMBX motility tracks by sub-pixel localization and linked these into trajectories (Arcizet et al., 2008; Tinevez et al., 2017)(Hafner et al., 2016; Zajac et al., 2013). The mean-squared displacements (MSDs) were compared as a function of time on a log-log plot, where a slope of  $\alpha=1$  indicates a purely diffusive process,  $\alpha<1$  in the case of confined diffusion, and  $\alpha=2$  in the case of processive transport (Arcizet et al., 2008); (Hafner et al., 2016; Ruthardt et al., 2011; Zajac et al., 2013). We repeated this fitting process in a sliding window along the trajectory to calculate a local slope or  $\alpha$ -value for each point in the trajectory (Figure 3A, Figure 3 figure supplement 1), and then used change-point analysis to identify segments of processive and paused motility (Beausang et al., 2011). The  $\alpha$ -value fluctuated between  $\sim 0$  and  $\sim 2$ , suggesting hMBX motors are either undergoing processive motility or remain tightly bound to single sites along MTs, without diffusing. We observe a bimodal  $\alpha$ -value distribution with peaks at  $0.627 \pm 0.041$  and  $1.760 \pm 0.041$  (Figure 3C). Our analysis suggests that hMBX motility changed significantly within a given trajectory between either paused or processive motile segments. The change point analysis likely underestimates of the number of short pauses. To account for pausing more effectively, we also fit the data for pauses  $\geq 5$  frames to a single exponential distribution, yielding a mean pause time of  $\sim 13.5$  s (Figure 3 figure supplement 1). The pause time distribution is described well by a single exponential. Quantifying the number of pauses per trajectory revealed that  $\sim 41\%$ ,  $\sim 27\%$ , and  $\sim 12\%$  of long trajectories contained zero, one, or two pauses, respectively (Figure 3 figure supplement 1). To allow for more averaging and minimize the effect of statistical fluctuations, we next calculated the MSD for all of the hMBX motility segments identified as paused or processive. As the localization error is most prominent at short timescales (Michalet, 2011) and is expected to be of a magnitude similar to the displacement of the motor due to directed motion in our experimental conditions, we focused our analysis on timescales of  $\sim 3$ -7 seconds (Duselder et al., 2015), also avoiding errors due to limited averaging at longer timescales (Michalet, 2011). The hMBX motor MSD curves exhibit two unique  $\alpha$ -values of 0.627 and 1.760 indicating either paused and processive motility trajectories, respectively (Figure 3C).

To determine the effect of the human Eg5 tail on motility properties of mini-tetramers, we compared hMBXt to hMBX motility independent of the change point analysis, we also calculated the MSD for all of the hMBXt motility events (paused and processive segments) and fit it to the function  $\langle r(\tau)^2 \rangle = (\phi v\tau)^2 + \phi 2D\tau + 2\epsilon^2$  where  $\phi$  is the fraction of time in the processive state (Chugh et al., 2018). From this global analysis, the fraction of time paused ( $1 - \phi$ ) is 0.47 for hMBXt compared to 0.03 for hMBX motors (Figure 3B). These results indicate that pauses are due to a statically bound state of the hMBX motor. For processive sections, the hMBX motors  $\alpha$ -value near 2 indicates that the motor's motility is dominated by active transport. Thus, our analysis suggests that hMBX motor paused states represent a single state that is tightly bound to MTs without diffusion. The hMBX motor motility velocity during processive motility segments displayed a single distribution (Figure 3D) ( $54.2 \pm 1.4$  nm/s). The velocity distribution for the paused fraction peaked near 0 nm/s ( $\mu = 3.9 \pm 1.8$  nm/s and  $\sigma = 52.3 \pm 1.3$  nm/s) suggesting clearly static motors that are strongly attached to MTs (Figure 3D).

Next, we analyzed the duration of hMBX processive motility events between paused states. We determined the distance travelled by a motor without pausing as the total run length. Since not all motile hMBX motors exhibited pauses, we observed two sub-populations: motors in which there was a pause, and motors in which the motility was uninterrupted. Correspondingly, distributions for total run lengths for hMBX motors were fit to a two-term exponential distribution,

261 with run lengths of  $554 \pm 60$ nm and  $2942 \pm 1106$ nm, with  $90 \pm 5\%$  of spots in the shorter run  
262 length population (Figure 3E). Plotting the inter-pause run lengths revealed a single exponential  
263 distribution with a mean run length of  $1263 \pm 167$ nm (Figure 3E, Figure 3 figure supplement 1).  
264 Thus, the shorter of the two estimates for total run lengths likely corresponds to the inter-pause  
265 run length or that of motors, which do not pause. This suggests that hMBXt motors may string  
266 together multiple shorter runs with pauses, allowing for a longer total run length. Both human  
267 and *Drosophila* mini-tetramers exhibit very similar pausing behavior (Figure 2C-D, G-H).  
268

269 To confirm the static nature of the hMBX pauses, we performed motility assays with the  
270 slowly hydrolysable ATP analog, AMPPNP, which is expected to trap motors in a strongly bound  
271 state (Chen et al., 2016). As expected, hMBX exhibited only static binding in the presence of  
272 AMPPNP (Figure 3 figure supplement 1) with normally distributed  $\alpha$ -value with a maximum near  
273 0.103 and a standard deviation 0.316, indicative of static binding (Figure 3 figure supplement 1).  
274 AMPPNP trapped hMBX motors show static binding similar to pauses observed in the presence  
275 of ATP. Thus, we propose that hMBX and kMBX motors switch between processive and static  
276 bound states, while moving along MTs toward plus-ends. We propose these paused states  
277 represent the nucleotide-free state rather than the ATP bound state, in both of which the motor  
278 domain has high affinity for MT lattice sites (Cross and McAinsh, 2014).  
279

### 280 **The kinesin-5 tail domain promotes motor clustering**

281  
282 Both kMBXt and hMBXt mini-tetramers formed multi-motor clusters along MTs during pauses  
283 (Figure 4A, B). Thus, we next analyzed the properties of these multi-motor clusters and how they  
284 form on MTs. First, we studied the role of electrostatic interactions in motor clustering and the  
285 impact of clustering on the motile properties of the motors. We compared kMBXt motor behavior  
286 across five ionic strength conditions (25, 50, 100, 125, 150 mM KCl) with the properties for kMBX  
287 motors in two ionic conditions (50 and 100 mM KCl) (Figure 4C). For each condition, we  
288 normalized the intensity of spots corresponding to motile motors along MTs visible in each field  
289 of view and analyzed the corresponding intensity distribution to determine the average intensity  
290 of individual mini-tetramer (Pandey et al., 2021)(Figure 4 figure supplement 1). The analysis  
291 revealed a major peak of spot intensity likely representing individual kMBXt mini-tetramers, but  
292 higher intensity spots were also observed, representing larger multi-motor clusters. We also  
293 determined the rate of kMBXt clustering formed during motility by measuring and quantifying the  
294 events in which motor intensities merged to form brighter spots, and quantified these events in  
295 the pools of motile motors in the different ionic strength conditions (Figure 4C). At 25-50 mM  
296 KCl, the majority of kMBXt motors formed clusters with either 2 (1+1) or 3(1+2), denoting the  
297 mini-tetramer ratio of motile motor to static motor (motile + static) components(Figure 4, figure  
298 supplement 2). However, at 50-150 mM KCl, a wider range of larger clusters was observed,  
299 representing 5-10 motors per cluster (1+4 to 2+10). We then calculated the total frequency for  
300 kMBXt cluster merging per unit MT length at 25-150 mM KCl, revealing the highest frequency  
301 peaks around 100 mM KCl, but this frequency is substantially lower at 25 mM or 150 mM KCl. In  
302 contrast few clustering events were observed for the KMBX motor in the absence of the tail  
303 domain at 50 and 100 mM KCl (Figure 4C). Thus, the kinesin-5 tail is responsible for kMBXt  
304 multi-motor clustering. At 25-50 mM KCl, clustering is likely low because the lower ionic  
305 strengths promote an intra-molecular tail-motor domain interaction due to their proximity. In  
306 contrast, at intermediate ionic strengths (100 mM KCl), the tail promotes interactions between  
307 multiple mini-tetramers and form clusters. At high ionic strengths (150 mM KCl), neither  
308 interaction is favored, again limiting the occurrence of interactions between mini-tetramers and  
309 thus diminishing the formation of clusters.  
310

311 Next, we studied the relationship between kMBXt motor cluster size and average velocity, run  
312 length and run time. At 25 and 50 mM KCl, run length and run time are shorter and correlated

313 with fewer motors per cluster. In contrast, at 100 and 125 mM KCl we observe an 80-100%  
314 increase in run length and run time and these features correlate with the larger motor-clusters.  
315 However, we found no direct correlation between cluster size and an increase in run length or  
316 run time within a single pool of motile kMBXt motors. Thus, our data demonstrate a critical role  
317 for the kinesin-5 tail mediated clustering in promoting slower motility and tight association with  
318 MT-plus ends. At lower ionic strength kMBXt motors behave more as individual tetrameric  
319 motors with shorter run lengths. At 100 mM KCl, kMBXt motor clustering becomes dramatically  
320 enhanced leading to motors that undergo motility more slowly with longer run lengths, run times.

321  
322 The hMBXt motile motors similarly formed clusters with paused hMBXt motor along MTs (Figure  
323 4A-B, Figure 4 figure supplement 1-3). To estimate more precisely the number of hMBXt motors  
324 in these clusters, we examined their spot intensities using multi-modal distribution analysis,  
325 revealing with a broad peak at ~6500au and peaks at 2 and 3 times this value (~13000au,  
326 ~19500au) (Figure 3D). The major peak likely represents individual hMBXt mini-tetramers, with  
327 the other peaks representing approximately 2 or 3 mini-tetramers. We tested the number of  
328 hMBXt motors in these clusters in the presence of AMPPNP, which led to non-motile attachment  
329 events. The spot intensity distribution for hMBXt in the presence of AMPPNP was predominantly  
330 unimodal (major peak at ~6100au and minor peak at ~13000au), suggesting that motility is  
331 required for hMBXt clusters to form along MTs (Figure 4E). In the presence of AMPPNP (i.e.  
332 without motor stepping), the major and minor peaks were clearly segregated; however, in the  
333 presence of ATP, these peaks were far less distinct (Figure 4D). This is likely because of the  
334 quenching and unquenching of the fluorophore pairs occurring with each step of the motor  
335 (multiple times during each frame) (Toprak et al., 2009). The multi-modal spot intensity  
336 distribution of hMBXt motors was similar to that of the hMBXt motors in the presence of  
337 AMPPNP, with a major peak at ~5300 au (Figure 4F). The small shift in intensity is likely due to  
338 a difference in TMR labeling ratios for the two constructs.

339  
340 Next, we measured the run length of hMBXt motor clusters moving along MTs (Figure  
341 4G). Quantifying the total run length of “clusters” (spots with an intensity  $\geq 1.5$ -fold higher than  
342 the mean intensity for single hMBXt tetramers) revealed run lengths of  $752 \pm 385$  nm and  $2443 \pm$   
343  $1649$  nm, similar to the run lengths of  $530 \pm 58$  nm and  $3112 \pm 1468$  nm for spots likely  
344 representing single hMBXt motors (Figure 4A). However, only  $7 \pm 4\%$  of single hMBXt motors  
345 were in the longer lifetime population, whereas  $36 \pm 40\%$  of hMBXt clusters were in this  
346 population. Additionally, many clusters reached the plus-ends of the MT on which they were  
347 moving, remaining bound at the MT plus-end. For very processive motors, the MT length has an  
348 effect on the measured run length distribution because many motors reach MT ends such as  
349 their runs are artificially truncated (McHugh et al., 2018; Thompson et al., 2013). Thus, we  
350 accounted for this censoring when fitting the run length distribution. Notably, satisfactory fits to  
351 either of the run length distributions, for either single motors or clusters could not be obtained  
352 using single exponential distributions, indicating that there is likely an inter-pause and total run  
353 length. Thus both single motors and clusters are able to string together runs with pauses.

354  
355 We subsequently analyzed the accumulation of hMBXt and kMBXt motors at MT plus  
356 ends. The hMBXt and kMBXt motors are highly processive, with run lengths that depend on the  
357 lengths of MTs, since many motors reach MT ends (McHugh et al., 2018). We observe an  
358 accumulation of both hMBXt and kMBXt motors at MT plus-ends, indicative of the stable  
359 association of tail-containing motors with MTs (Figure 4A). We quantified the dwell times of  
360 hMBXt motors at MT plus ends by measuring the intensity in a region centered at the plus-end of  
361 each MT and defining the period of time for which the intensity was  $>3$  standard deviations  
362 above the background signal as the cluster lifetime. The tail domain enables mini-tetramers to  
363 maintain association at MT plus ends, where hMBXt motors pause for  $\sim 10x$  as long as hMBX  
364 motors (Figure 4H, I). For hMBXt, we could not obtain a satisfactory fit to cluster lifetimes using a

365 single Weibull distribution, prompting us to use a mixed Weibull distribution with dwell-times of  
366  $16.4 \pm 4.9$  seconds and  $483.7 \pm 153.2$  seconds (Figure 4I, Figure 4 figure supplement 5). This  
367 suggests the presence of two populations of plus-end clusters with different dwell times, with  $49$   
368  $\pm 15\%$  of motors in the shorter lifetime population. Next, we analyzed cluster lifetimes as a  
369 function of the intensity of the first 5 frames of that end cluster, revealing that motors that arrived  
370 in a cluster that had “pre-formed” along the MT were likely to remain associated with the plus-  
371 end (Figure 4J). We used this measure of the starting spot intensity rather than the mean spot  
372 intensity to distinguish between motors arriving in “pre-formed” clusters and motors arriving  
373 individually and gradually forming a cluster at MT plus-end. The arrival of “pre-formed” clusters  
374 was supported by the observation that intensity traces in the region near MT plus-ends generally  
375 increased above baseline or decreased to baseline in one or a few frames, regardless of the  
376 plateau intensity (Figure 4J, Figure 4 figure supplement 6). Thus, the shorter lifetime likely  
377 represents the dwell time of single hMBXt motors at the ends of MTs, while the longer lifetime  
378 likely represents that of clusters.  
379

380 The hMBX motors did not accumulate as robustly at MT plus-ends (Figure 4I). The dwell  
381 times of hMBX motors at the plus-ends of MTs were  $14.6 \pm 3.2$  seconds and  $139.9 \pm 137.5$   
382 seconds, with  $74 \pm 18\%$  of motors in the shorter lifetime population (Figure 4I, Figure 4 figure  
383 supplement 4). Thus, the shorter dwell times for hMBX and hMBXt clusters are similar, in  
384 agreement with the idea that this represents the lifetime of single motors (present for both  
385 constructs) at MT plus-ends. In contrast, the longer lifetimes are shorter for hMBX motors, and a  
386 smaller fraction of motors is likely to be in this longer dwell-time subpopulation, indicating that  
387 the inability of hMBX motors to cluster may prevent them from remaining bound at MT plus-ends  
388 for extended periods (Figure 4H, I, J). To determine the possibility of hMBXt clusters reaching  
389 MT plus-ends, we next compared the distribution of frame-to-frame velocities for single motors  
390 and clusters in the paused and processive states (Figure 4). Our analysis agrees with the visual  
391 observations, that hMBXt clusters move more slowly than single hMBXt motors: whereas the  
392 mean paused velocities of single motors ( $4.6 \pm 3.1$  nm/s and  $\sigma = 64.8 \pm 2.2$  nm/s) and clusters  
393 ( $3.6 \pm 1.9$  nm/s and  $\sigma = 37.6 \pm 1.3$  nm/s) were similar, the processive velocity of single motors  
394 ( $63.3 \pm 2.3$  nm/s) was higher than that of clusters ( $43.2 \pm 1.6$  nm/s). Additionally, the velocity of  
395 single motors was more variable than that of clusters. During the processive sections of  
396 trajectories, the standard deviation of single motor velocities was  $65.3 \pm 1.6$  nm/s, whereas that  
397 of clusters was  $39.5 \pm 1.2$  nm/s. This might contribute to the observation that the velocity of  
398 hMBXt motors ( $54.2 \pm 1.0$  nm/s) is slower than that of hMBX motors ( $80.4 \pm 4.4$  nm/s).  
399

400 We also measured the average dwell time for ensembles of kMBX and kMBXt motors at  
401 MT plus ends in different ionic strength conditions. We observe that kMBX motors dwell at MT  
402 ends for  $78 \pm 19$  s at 50 mM KCl and for  $25 \pm 18$  s at 100 mM KCl, showing a three-fold  
403 decrease upon ionic strength increase (Figure 4K). In contrast kMBXt motors show consistently  
404 longer dwell time at MT plus-ends, which is two-three folds higher than kMBX motors (125 to  
405 250 s), and are not influenced by changes in ionic strength (25- 150 mM KCl) (Figure 4K). The  
406 majority of kMBXt clustering events also correlate with the motors arriving at MT plus-ends  
407 particularly at 100 mM KCl condition. This is likely due to the enhanced multi-motor clustering  
408 coupled with the enhanced dwell time at MT plus-ends at 100 mM KCl. Our data suggests that  
409 the MT plus-end dwell time is likely related to the motors pausing at MT plus-ends, and that the  
410 tail enhances this property by down-regulating the ATP hydrolysis activity of the motor domain.  
411

### 412 **Short kinesin-5 mini-tetramers show unique MT crosslinking and MT sliding features**

413  
414 We next sought to determine whether kinesin-5 mini-tetramers are capable of crosslinking,  
415 aligning, and sliding pairs of MTs. To do this, we immobilized taxol-stabilized HiLyte 646 and  
416 biotin labeled MTs on a coverslip via a streptavidin-biotin linkage. We found that to achieve



417 efficient MT bundling, particularly for the mini-tetramer motors, we required high velocity flow of  
418 MTs in flow cells such that they were well nearly aligned with the direction of flow. Next, motors  
419 were introduced into the sample chamber at a specified concentration and allowed to decorate  
420 the coverslip-attached MTs. Finally, Rhodamine-labeled MTs and ATP were introduced with  
421 rapid flow rates, and kinesin-5 mediated crosslinked MT bundles were allowed to form and  
422 motors to initiate relative MT sliding. We then imaged both the coverslip attached MT, paired  
423 MTs and kinesin-5 motors using the three different channels via TIRF microscopy at 2-5 sec  
424 frame rates.

425  
426 We first set out to determine how efficiently four different kinesin-5 motor constructs can  
427 crosslink and pair MTs, by comparison: full-length Eg5 with tail (hFLt), full-length Eg5 without the  
428 tail (hFL), previously prepared as described (Bodrug et al., 2020), kinesin-5 mini-tetramer with  
429 tail (kMBXt), and kinesin-5 mini-tetramer without tail (kMBX). We then imaged multiple fields-of-  
430 view immediately after flowing in ATP and Rhodamine-MTs and measured how many MT  
431 bundles had formed relative to the population of surface-bound MTs (Figure 6a-b). We found  
432 that both hFLt and hFL motor constructs recruited free MTs from solution, forming MT pairs that  
433 underwent sliding at relatively high rates, with  $63\pm 5\%$  and  $54\pm 16\%$  in the hFLt and hFL motor  
434 conditions, respectively. This consistent with observations we made previously at similar  
435 concentrations (Bodrug et al., 2020). In contrast, the kMBXt motor formed MT bundles 3-fold  
436 less frequently ( $24\pm 14\%$ ) compared to hFLt, while the kMBX almost never recruited a free MT  
437 from solution and rarely formed MT pairs, with only 2% of all surface MTs observed to bundle a  
438 second MT (Figure 5A-B). Together, these data suggest that the kinesin-5 mini-tetramer motors  
439 are less efficient than the full-length kinesin-5 motors at spontaneously forming antiparallel MT  
440 bundles and that the tail domain is critical for establishing the MT crosslinked geometries,  
441 especially in the mini-tetramer constructs.

442  
443 We next sought to determine how kinesin-5 mini-tetramers compared to full-length kinesin-5 in  
444 MT crosslinking, pairing or alignment and then MT sliding. We therefore monitored the positions  
445 of the mobile MT and the full length or mini-tetramer kinesin-5 motors during these sliding events  
446 across a range of conditions. As we were unable to form bundles using kMBX motor in our  
447 assays, we focused on comparing the mechanics of the full-length (hFLt) motor and mini-  
448 tetramer motor (kMBXt) both of which contain kinesin-5 tail domains. Both motors were able to  
449 slide MTs apart efficiently (Figure 5C). Interestingly, kMBXt motor appeared less mobile and  
450 more clustered relative to the hFLt motor along the MTs throughout MT sliding events (Figure  
451 6c). We also observed that the mobile free-MT occasionally paused or exhibited reduced  
452 velocity for brief stretches when undergoing sliding by the full-length kinesin-5 (hFLt). In contrast,  
453 MT sliding generated by kMBXt motor tended to exhibit more consistently continuous MT sliding  
454 motility with faster velocities throughout (Figure 5C). To examine this difference, we determined  
455 the frequency of observed pauses or velocity decreases across many MT sliding examples and  
456 found that MT bundles in the full length kinesin-5 (hFLt) condition exhibited pauses  $0.21\pm 0.06$   
457 times per micron ( $\mu\text{m}$ ) of distance travelled, while kinesin-5 mini-tetramer (kMBXt) paused at a  
458 lower rate of  $0.08\pm 0.04$  times per micron ( $\mu\text{m}$ ) which is three-folds lower than the pausing  
459 exhibited by full length (hFLt) motor MT sliding (Figure 5D). Finally, we calculated the MT sliding  
460 velocity across a range of ATP concentrations for both constructs (Figure 5E). We found that the  
461 MT sliding velocity was approximately twice the speed of single motor stepping motor velocity,  
462 consistent with the previously reported finding that both pairs of motor domains at each of the  
463 bipolar end of kinesin-5 motors are stepping along their respective MT in the opposite direction,  
464 leading to a two-fold MT sliding motility compared to the motility generated along single MTs  
465 (Kapitein et al., 2005). Importantly, we observed that the average velocity of kinesin-5 mini-  
466 tetramer (kMBXt)-driven MT sliding at 100 and 250  $\mu\text{M}$  ATP was about 10% higher than that of  
467 full-length kinesin (hFLt)(table 3). Together, these results indicate that, while the kinesin-5 mini-  
468 tetramers are not as efficient at initially crosslinking aligning two MTs as native kinesin-5, they

469 are capable at sliding MTs, doing so within clusters, with less three-fold less pausing and 10%  
470 higher velocities compared to those generated by full-length kinesin-5.

471  
472

## 473 **Discussion**

474

475 Human cells encode 45 kinesin motors, each of which is adapted to perform a unique set of  
476 cellular functions. This functional diversity is demonstrated beautifully in the mitotic spindle,  
477 where kinesins perform diverse tasks ranging from regulating dynamics to crosslinking and  
478 sliding MTs. To fulfill their functional niches in mitosis, kinesins have evolved biophysical and  
479 biochemical differences that render them uniquely well-suited for these roles. Through  
480 comparing the motility and structure of full-length and minimal tetrameric kinesin-5 motors, our  
481 studies reveal the role of the C-terminal tail and bipolar tetrameric minifilament domains in  
482 governing kinesin-5 motor clustering and MT sliding motility. The structural and biochemical  
483 features of these domains are highly conserved across all the kinesin-5 motors. Our structure of  
484 the extended kinesin-5 BASS domain reveals that it possesses the unique capacity to form a  
485 force-bearing junction for two pairs of motors positioned at opposite ends of its bipolar structure.  
486 We designed and studied Human and *Drosophila* kinesin-5 mini-tetramer motors based on the  
487 BASS-XL x-ray structure (Figure 1), which recapitulate critical aspects but reveal unique  
488 differences compared to full-length kinesin-5 motor motility (Bodrug et al., 2020). These  
489 structural adaptations are critical for kinesin-5 function in bipolar mitotic spindle assembly,  
490 organization, and elongation.

491

### 492 **The kinesin-5 tail domain binding regulates the motor domain mechanochemical cycle** 493 **and promotes slower motility and increased processivity.**

494

495 The kinesin-5 tail domains down-regulate MT activated motor domain ATP hydrolysis by  
496 stabilizing the MT bound nucleotide free state. This interaction leads to slower stepping during  
497 processive motility, longer run lengths, and frequent pauses (Figure 2-3). As with full length  
498 kinesin-5 (Bodrug et al., 2020), the presence of the tail domains in both *Drosophila* and human  
499 mini-tetramers leads to slow motility with multiple pauses in which motors are statically bound to  
500 MTs (Fig. 2). The pauses represent strongly-bound states with extended lifetimes in which the  
501 leading motor domain is in the no nucleotide state, while and the trailing motor domain is either  
502 in the ADP-P<sub>i</sub> or ADP state, similar to the so-called ATP gate or stepping gate (Andreasson et  
503 al., 2012; Bodrug et al., 2020; Cross and McAinsh, 2014). This is similar to motor motility in the  
504 presence of a mixture of ATP and AMP-PNP, in which comparable switches in motility are  
505 observed (Subramanian and Gelles, 2007; Vugmeyster et al., 1998). We suggest that the  
506 kinesin-5 tail domain docking onto the motor domain serves as an externally imposed gate to  
507 organize multiple kinesin-5 motors in clustered assemblies. The kinesin-5 tail domain enhances  
508 the pausing and promotes motor assembly into clusters via encounters between motile and  
509 paused motors along MTs. The tail to motor trans-interactions between the tails of one kinesin-5  
510 tetramer and the motor domains of other tetramers. Interestingly, motor clustering has also been  
511 described for the budding yeast, *Saccharomyces cerevisiae*, ortholog Cin8 and has been  
512 proposed to mediate its minus-end to plus-end MT motility directionality reversal (Pandey et al.,  
513 2021a; Pandey et al., 2021b; Shapira et al., 2017; Singh et al., 2018).

514

### 515 **The kinesin-5 tail domain drives the formation of multi-motor clusters with different** 516 **motile properties than single motors**

517

518 Our studies of *Drosophila* and human kinesin-5 mini-tetramers reveal that tail to motor domain  
519 interaction is highly conserved, in which the tail domains induce pausing and drive kinesin-5  
520 motors to assemble into multi-motor clusters. By increasing the pause frequency, the tail domain

521 increases the frequency of encounters between motile and paused motors, allowing for the  
522 formation of multi-motor clusters mediated by trans-interactions between the tails of one  
523 tetramer and the motor domains of other tetramers (Bodrug et al., 2020). The tail to motor  
524 interaction leads to a decrease in overall motility velocities. Within clusters, multiple motors  
525 move together as assemblies (Figure 4). The tail may stochastically dissociate from the front  
526 motor domain, allowing the motor domains to continue stepping. The increase in the number of  
527 motors in these clusters likely leads to longer run lengths likely due to the increase in the  
528 numbers of stepping motors domains. Indeed, we observed an increased total run lengths in  
529 kMBXt and hMBXt motors compared to kMBX and hMBX motors, supporting the effect of the tail  
530 on increasing processive run lengths. The lifetime of motors at MT plus-ends is related to the  
531 number of motors in the clusters that arrive. The kMBX or hMBX motors generally dissociate  
532 from the MT plus-end more quickly than clusters of kMBXt or hMBXt motors (Figure 4).  
533 Additionally, kMBXt or hMBXt motor clusters were found to move at slower and less variable  
534 speeds than single motors (Figure 4). Clusters and single motors may be fulfilling different roles  
535 during spindle assembly. Clusters of motors may be present between parallel MTs, such as near  
536 the spindle poles, where, because of their increased association time with MTs, they could assist  
537 in MT capture early in spindle assembly. Kinesin-5 clusters may be selectively retained in this  
538 region because they move slower than single motors (Fig. 4). In contrast, faster moving single  
539 motors may “escape” and travel towards MT plus-ends, localizing them in the region of  
540 antiparallel MT overlap in the spindle midzone. Here, they could facilitate spindle pole separation  
541 and/or regulate the rate at which this occurs

542  
543 **The kinesin-5 tail-motor interaction is likely tuned by mitotic phosphorylation of the**  
544 **conserved BimC box in the tail domain.**

545  
546 The kinesin-5 tail domain contains a conserved BimC box or CDK1 phosphorylation site  
547 (Threonine 926 in human kinesin-5) and the more distal regulatory regions of the tail domain (i.e.  
548 the KEN box, D box, and Nek6 phosphorylation site (Blangy et al., 1995)(Bertran et al., 2011;  
549 Drosopoulos et al., 2014; Rapley et al., 2008). In particular, the phosphorylation of the kinesin-5  
550 tail by Cdk1 kinase has been shown to increase the affinity of the motor for MTs *in vitro* (Cahu et  
551 al., 2008). Based on our observations, we hypothesize that such phosphorylation may enhance  
552 the tail-motor interaction by adding a negative charge to the tail, potentially increasing its affinity  
553 for the motor domain, which is positively charged near the ATP binding site. The CDK1  
554 phosphorylation of the tail domain could act to increase the affinity of the motor for MTs by  
555 promoting tail docking, hereby increasing the time that the motor spends in its strongly-bound  
556 state. The enhancement of the tail regulation may lead to changes in the MT sliding mechanism  
557 or enhancing the brake function for kinesin-5 during anaphase. The impact of phosphorylation of  
558 the kinesin-5 tail warrants further study.

559  
560 **The tail to motor interaction supports kinesin-5’s function as a brake during mitosis**

561 Kinesin-5 motors have been suggested to act as a brake to slow the rate of MT sliding by other  
562 motors, both during anaphase (Rozelle et al., 2011; Saunders et al., 2007) and in non-mitotic  
563 cells (Falnikar et al., 2011; Lin et al., 2011; Myers and Baas, 2007; Nadar et al., 2008; Nadar et  
564 al., 2012). Moreover, the ability of kinesin-5 motors to act as a brake between parallel MT or  
565 quickly sliding antiparallel MTs has been demonstrated *in vitro* (Shimamoto et al., 2015). The tail  
566 docking onto the motor domain to induce pausing and motor clustering may contribute to the  
567 capacity of kinesin-5’s brake-like behavior by increasing the time these motors spend in their  
568 strongly bound state on the MT lattice. This would allow the motor to prevent rapid sliding of two  
569 MTs in a parallel orientation. The tail’s regulation is critical for optimal force transmission through  
570 kinesin-5 minifilaments to promote efficient crosslinking and sliding. We expect that a motor is  
571 less likely to detach when subject to loads while in tail-induced clustered and paused states than  
572 while moving processively as individual tetramers. The paused state of clustered motors would

573 be particularly strongly attached to MTs, allowing them to withstand substantial loads when  
574 acting as a brake.

575  
576 **Clusters of Kinesin-5 remain stably associated with the plus-ends of stabilized MTs**  
577 Kinesin-5 clusters often reached MT plus ends and they remained bound for extended periods of  
578 time (Figure 4). The tail to motor interaction strongly enhances the kinesin-5 the MT plus-end  
579 association. The accumulation of kinesin-5 at MT plus-ends has been described previously  
580 (Chen & Hancock, 2015; Kapitein et al., 2005). We interpret this MT plus-end accumulation to be  
581 due to the extended lifetime of kinesin-5 strongly-bound motor states, compounded by tail to  
582 motor interaction enhancing the binding affinities of the motors and enhancing their clustering  
583 (Furuta et al., 2013; Vershinin et al., 2007). Indeed, we observed that the motors that arrived at  
584 MT ends in clusters remained bound for longer periods of time (Figure 6c). In contrast to  
585 previous reports employing dimeric kinesin-5 constructs, it has proposed that this MT plus-end  
586 accumulation reveals a role for kinesin-5 motor domain in modulating MT dynamics (Chen et al.,  
587 2019; Chen and Hancock, 2015). However, we find that kinesin-5 mini-tetramers lacking the tail  
588 domain have short life times at MT plus ends, likely due to tail to motor interaction stabilizing the  
589 high affinity motor states and inducing multi-motor clusters. Furthermore kinesin-5 cluster also  
590 move with a slow velocity of ~43nm/s, which may be too slow to allow them to accumulate at the  
591 ends of dynamic MTs within the spindle.

592  
593 **The length of the Kinesin-5 central minifilament directly regulates force transmission**  
594 **during MT sliding motility**

595 Our studies help to elucidate the crucial role of the 60-80 nm Kinesin-5 minifilament in the  
596 kinesin-5 MT sliding mechanism. We compared kinesin-5 mini-tetramers with full-length kinesin-  
597 5 motors to determine the relationship between the length of the kinesin-5 minifilament to the  
598 efficiency of MT pair formation, and its impact on MT sliding motility activities. The kinesin-5  
599 mini-tetramers are half the length of native kinesin-5 motors. The short minifilaments in kinesin-5  
600 mini-tetramers are stiffer due to the shorter dimeric coiled-coils on either side of the BASS  
601 domain. This leads to low torsional flexibility and therefore enhance the force coupling between  
602 the bipolar ends of kinesin-5 as they engage the two MTs they crosslink. However, the  
603 decreased flexibility either end of the kinesin-5 mini-tetramers appears to impede efficient MT  
604 alignment into bundles. In particular, this decreased flexibility leads to defects in the initial  
605 crosslinking of MT pairs prior to MT sliding. Once crosslinked and aligned, however, the shorter  
606 minifilament leads to a higher maximal MT sliding velocity compared to native kinesin-5 due to  
607 the increased stiffness of kinesin-5 minitetramers.

608  
609 Our studies also show the relationship between the kinesin-5 minifilament length and the motor  
610 to tail regulation in modulating MT sliding motility. The decreased kinesin-5 minifilament torsional  
611 flexibility in the mini-tetramer motors leads to dependence on the tail-motor regulation during MT  
612 crosslinking, alignment and sliding in contrast to full-length kinesin-5, where the tail was not  
613 strictly required *in vitro*. The kinesin-5 mini-tetramers show a very poor capacity to assemble  
614 paired sliding MTs in contrast to the full-length kinesin-5 motors such as the hFL ( $\Delta$ tail kinesin-  
615 5), which assembles MT sliding pairs, but with decreased efficiency relative to the hFLt (full  
616 length kinesin-5)(Bodrug et al., 2020). These data also show that the tail-motor regulation  
617 enhances force transmission properties of kinesin-5 engaged motor ends, and that the motility  
618 resulting forces are transmitted between kinesin-5 bipolar ends via their central tetrameric  
619 minifilaments.

620  
621 Taken together, our studies identify how the unique structural adaptations of the kinesin-5 tail  
622 and tetramerization domains enable its role in organizing the mitotic spindle. The tail domain  
623 promotes motor pausing and clustering. Single motors and clusters behave differently,

624 suggesting that they may fulfill different roles in spindle assembly. The length of the minifilament  
625 contributes flexibility to enable kinesin-5 to initiate MT crosslinking efficiently.  
626  
627

628 **Acknowledgement**

629  
630 The authors thank Dr Jonathan Scholey (Molecular Cellular Biology, UC-Davis) for the  
631 inspiration on the project. J.A.B thanks Dr. Richard Mckenney (Molecular Cellular biology, UC-  
632 Davis) for the critical reading of this manuscript. BASS-XL diffraction data were collected at the  
633 Stanford Radiation Laboratory (SSRL) using 11-1 beamline. We thank Peter Dunten, Ana  
634 Gonzalez, and Tzanko Doukov (SSRL) for help with data collection. This research was  
635 supported in part by the Israel Science Foundation grant (ISF-386/18) awarded to L.G.; the  
636 National Science Foundation (NSF-1615991) and United States - Israel Binational Science  
637 Foundation grant (BSF-2015851), awarded to L.G. and J.A.B., respectively; A United States -  
638 Israel Binational Science Foundation grant (BSF-2019008), awarded to L.G. and S.R.; and the  
639 National Institutes of Health (NIH- GM11283), awarded to J.A.B. S.F is supported by the  
640 Rensselaer Polytechnic Institute School of Science Startup funds. A.G.H is supported by the  
641 Canadian Institutes of Health Research (CIHR) grant PJT-159490 and the Natural Sciences and  
642 Engineering Research Council of Canada (NSERC) grant RGPIN-2020-04608. Crystallographic  
643 data and Structure coordinates are deposited at the RCSB (PDB ID: 7S5U).

## 644 **Materials and Methods**

645

### 646 **Protein Production, X-ray crystallography and Model building.**

647

648 The KLP61F minifilament extended region (residues 597-833) was expressed and purified in  
649 BL21 *E. coli* as described in Scholey et al 2014. Bacterial pellets were lysed using a micro-  
650 fluidizer in (300 mM KCl, 50 mM HEPES, 1 mM MgCl<sub>2</sub>, 3 mM β-mercaptoethanol with protease  
651 inhibitors). The bacterial lysate was clarified by centrifugation at 18k rpm for 30 min at 4°C. Ni-  
652 NTA affinity was used to purify BASS-XL, and passage over HiTrap Q HP cation exchange in  
653 low salt (70 mM KCl, 50 mM HEPES, 1 mM MgCl<sub>2</sub>) was used to remove contaminants where  
654 BASS-XL eluted in the flow through. A second Ni-NTA affinity step was used in conjunction with  
655 10K Amicon Filters to concentrate the BASS-XL. The concentrated BASS-XL tetramer was  
656 applied on a HiLoad 16/600 Superdex 200 gel filtration column using an AKTA Purifier (GE  
657 Healthcare). Crystallization conditions were screened using a Mosquito Robot (TTP Labtech) by  
658 mixing a 100 nL of protein with 100 nL precipitant conditions. Crystals were obtained and  
659 refined in 0.01 M FeCl<sub>3</sub>, 0.1M sodium citrate pH 5.6, 12% Jeffamine M-600 at 18°C and  
660 cryoprotected with 20% glycerol. Crystals were diffracted at the SSRL 11-1 beamline and  
661 showed highly anisotropic x-ray diffraction. Crystals adopt space group C2 with four molecules  
662 in the asymmetric unit. We used 4.4 Å as the high-resolution cut-off to avoid excessive loss of  
663 completeness. The diffraction data was truncated using boundaries determined via the  
664 Anisotropic server (Strong et al., 2006). The BASS-XL structure was determined using molecular  
665 replacement using the previously determined BASS model (Scholey et al 2014). Data from each  
666 monomer were combined using non-crystallographic symmetry and were averaged and refined  
667 using PHENIX with cycles of model building using coot program (Emsley et al., 2010; Liebschner et  
668 al., 2019). The individual positional coordinates and anisotropic B-factor were refined with  
669 automatic weight optimization in the final stage. The final model includes BASS core domain  
670 with extended parallel helices at the N-terminal end.

671

### 672 **Engineering *Drosophila* and human mini-tetramer kinesin-5 motors**

673

674 Human and *Drosophila* kinesin-5 mini-tetramers were designed using the BASS-XL x-ray  
675 structure as a template. For the KLP61F KMBX and KMBXt mini-tetramer constructs, the BASS  
676 XL was extended by 20 residues based on the heptad pattern observed in BASS-XL the  
677 structure (residues 597-833) and fused at its N-terminal end to the KLP61F motor and neck  
678 linker domain (residues 1-369) and were either contained or lacked a C-terminal extension of the  
679 KLP61F tail domain (residues 910-1066) with a C-terminal his tag. For the Eg5 mini-tetramer  
680 hMBX and hMBXt constructs the *Homo sapiens* Eg5 motor domain and neck linker (1-374) were  
681 fused to the N-terminal end of the *Drosophila melanogaster* BASS-XL domain (597-799), either  
682 contained or lacked the *Homo sapiens* Eg5 C-terminal tail domain (913-1056), and a C-terminal  
683 6x-His tag with mutations (C25V, C43S, C87A, C99A, N358C, C964S, and C1003S) to allow for  
684 the specific labeling of the motor at a single reactive cysteine residue in the neck linker (N358C).  
685 Tubulin was purified from Pork or Bovine brains (Castoldi and Popov, 2003). After purification,  
686 tubulin was cycled or labeled (with Alexa-546 or Alexa 647 (Thermo Fisher Scientific; Waltham  
687 MA), HiLyte 488 (AnaSpec; Fremont CA) or Biotin-LC-NHS (Thermo Fisher Scientific)) and then  
688 cycled prior to use. Unless otherwise stated, all chemicals and proteins were purchased from  
689 MilliporeSigma (Burlington, MA).

690

### 691 **Motility assays for *Drosophila* Kinesin-5 (kMBX and kMBXt) minitetramers**

692

693 Flow chambers were assembled from N 1.5 glass coverslips (0.16 mm thick; Ted Pella) that  
694 were cleaned with the Piranha protocol and functionalized with 2 mg/mL PEG-2000-silane  
695 containing 2 µg/mL biotin-PEG-3400-silane (Laysan Bio) suspended in 80% at pH 1 (Henty-

696 Ridilla et al., 2016). After the flow chamber was assembled, 0.1 mg/mL NeutrAvidin  
697 (ThermoFisher) was used to functionalize surfaces. Biotin and Alexa-Fluor-633-labeled porcine  
698 tubulin were generated in the laboratory as described (Al-Bassam, 2014) and were polymerized  
699 using the non-hydrolysable GTP analog guanosine-5'-[( $\alpha,\beta$ )-methylene] triphosphate (termed  
700 GMPCPP; Jena Biosciences) or using the MT stabilizing drug, Paclitaxel (sigma). These MTs  
701 (100–200  $\mu\text{g}/\text{mL}$  in BRB-80: 80 mM PIPES, 1 mM  $\text{MgCl}_2$  and 1 mM ETGA; pH 6.8, 1% glycerol,  
702 0.5% pluronic-F127, 0.3 mg/ml casein, 3 mM BME, 4 mM ATP- $\text{MgCl}_2$ ) were flowed into  
703 chambers and attached to glass via biotin-neutravidin linkage. Flow chambers were then  
704 extensively washed with imaging buffer (25 mM HEPES, 25–150 mM KCl, pH 7.5, 10 mM beta-  
705 mercatopethanol; 1% glycerol, 0.5% Pluronic-F127, 0.3 mg/ml casein, 3 mM BME, 4 mM ATP-  
706  $\text{MgCl}_2$ ). Kinesin-5 MT-stimulated motility was reconstituted at 25°C by injecting 1–20 nM FL-  
707 Eg5-GFP combined with a photo-bleach-correction mixture into flow chambers (Telley et al.,  
708 2011). Movies were captured in TIRF mode using a Nikon Eclipse Ti microscope using 1.5 Na  
709 objective and an Andor IXon3 EM-CCD operating with three (488 nm, 560 nm and 640 nm)  
710 emission filters using alternating filter wheel in 2 s increments operated using elements software  
711 (Nikon).

712

### 713 **Motility assays for human Kinesin-5 (hMBX and hMBXt) mini-tetramers**

714

715 Coverslips (22x30mm; Thermo Fisher Scientific) were cleaned by soaking in acetone for 10  
716 minutes, sonicating in 50% methanol for 20 minutes, sonicating in 0.5M KOH for 20 minutes,  
717 and then rinsing in MilliQ water three times before drying using nitrogen gas. Cleaned coverslips  
718 were stored covered at room temperature. Immediately prior to silanization, coverslips were  
719 plasma treated on “high” (~18W; 200mTorr) for 45 seconds after evacuating the chamber.  
720 Subsequently, they were soaked in PlusOne Repel-Silane ES (GE Healthcare; Chicago IL) for  
721 20 minutes, transferred to 95% ethanol for 5 minutes, and then sonicated in fresh 95% ethanol  
722 for 10 minutes. Finally, they were dried again using nitrogen gas and stored covered at room  
723 temperature for up to 2 months.

724 Taxol-stabilized MTs were prepared as follows: purified unlabeled, Alexa 647-labelled, and  
725 biotinylated tubulin were combined at 50 $\mu\text{M}$  in BRB80 in a 50:2:1.5 ratio and supplemented with  
726 2mM GTP. After incubating at 37°C for 40 minutes, 40 $\mu\text{M}$  Taxol (Cytoskeleton; Denver CO) was  
727 added, and MTs were incubated for an additional 30 minutes. Subsequently, MTs were pelleted  
728 by centrifugation (8000 rcf, 10 minutes, 25°C), and, after washing the pellet, resuspended in  
729 fresh BRB80 supplemented with 40 $\mu\text{M}$  Taxol. The pelleting, washing, and resuspension were  
730 repeated twice sequentially.

731 Single molecule motility assays were carried out as follows: Flow chambers with a volume of  
732 ~20 $\mu\text{L}$  were prepared from a silanized coverslip, a glass slide, and double-sided tape.  
733 NeutraAvidin was introduced at 20 $\mu\text{g}/\text{mL}$  and incubated for 5 minutes, before blocking the  
734 remaining surface using 50mg/mL Pluronic F-127 for 30 minutes. Stabilized MTs containing  
735 biotinylated tubulin were then flowed in at a concentration of ~0.14mg/mL and allowed to bind for  
736 5 minutes, at which point any unbound MTs were removed by washing the chamber with BRB80  
737 supplemented with 20 $\mu\text{M}$  Taxol. Just prior to imaging, the assay buffer consisting of BRB80  
738 supplemented with 20 $\mu\text{M}$  Taxol, 0.5mg/mL BSA, 10mM DTT, 2mM ATP, 0.5mg/mL glucose  
739 oxidase, 7mg/mL glucose, 0.2mg/mL catalase, 0.2%w/v PEG, 40mM potassium acetate, and  
740 ~22nM kinesin-5 (with or without the tail) was introduced. The flow chamber was then sealed at  
741 either end using vacuum grease and imaged immediately for no more than 30 minutes. Assays  
742 with AMP-PNP were performed identically, except that motors were diluted 36x more and the  
743 ATP was substituted with 2mM AMP-PNP (Roche Diagnostics; Indianapolis IN).

744 TIRF microscopy imaging was performed using an Eclipse Ti-E inverted microscope (Nikon;  
745 Melville NY) equipped with diode lasers (100mW; 405nm, 488nm, 561nm, and 640nm)  
746 (Coherent; Santa Clara CA), custom optics for TIRF, a 1.49 NA 100x objective, and an additional  
747 1.5X lens to increase the magnification. Two-color image series were acquired by capturing



748 images of the MTs (640nm, 100ms exposure, 1mW) and the motors (561nm, 200ms exposure,  
749 2mW) in an alternating fashion by alternating the laser illumination in synchrony with the rotating  
750 filter wheel using a custom-written LabView program, resulting in a frame rate of  $\sim 1.2\text{s}^{-1}$ . Images  
751 were captured on an iXon U897 EMCCD camera (Andor Technology; South Windsor CT).

752

### 753 **Single Molecule Analyses for *Drosophila* kinesin-5 (kMBX and kMBXt)**

754

755 Motility, run length and run time analyses were carried out as follows: Image movie stacks were  
756 pre-processed with photobleach correction and image stabilization plugins using the program  
757 FIJI (Schindelin et al., 2012). For motility along individual MTs, individual kMBX and kMBXt  
758 motor motility events were identified along anchored MTs based on kymographs in generated for  
759 multiple channels. The FIJI kymograph TrackMate plugins (Schindelin et al., 2012) were used to  
760 measure particle motility rates, identify their run lengths as and run time. Large collections of  
761 motile events along fields of MTs were collected for kMBXt motors at 25, 50, and 100, 125 and  
762 150 mM KCl conditions and collected for kMBX motors at 50 and 100 mM KCl conditions (Table  
763 2). Average MT parameters were determined by frequency binning the motility events in a range  
764 conditions and then fitting these events using Gaussian distributions using the program Prism  
765 (Table 2). In general, all parameters fit single Gaussian distributions. Run lengths were fitted  
766 using exponential decay to identify the half-length for each motor condition. T-tests were  
767 performed to determine significance of the differences observed.

768 The stoichiometry of kMBX and kMBXt motors per multi-motor cluster were determined as  
769 previously described (Pandey et al., 2021). Briefly, following correction for the uneven  
770 illumination of images and background subtraction, intensities of all NG-labeled kMBX or kMBXt  
771 in the first frame of a time-lapse sequence were measured using the TrackMate plugin of the  
772 ImageJ-Fiji software (Schindelin et al., 2012; Tinevez et al., 2017). Since kMBX and kMBXt are  
773 homo-tetrameric, each motor contains at least four NGs per tetrameric motor. The major peak of  
774 the intensity distribution histogram of these mNG-labeled mini-tetramers was fitted to a Gaussian  
775 distribution. The center of the Gaussian peak lay at  $\sim 600$  a.u., which corresponds to the average  
776 intensity of single kMBX or kMBXt motor containing one, two, three, or four fluorescent mNG,  
777 with each fluorescent mNG molecule contributing  $\sim 240$  a.u. to the total intensity. Thus, the neon  
778 green labeled motor population within this Gaussian peak likely represents single kMBX or  
779 kMBXt motors. By this method, we assigned intensity ranges for kMBX or kMBXt molecules  
780 fluorescence as  $<960$ ,  $960-1920$  and  $>1920$  for single mini-tetramer, pairs mini-tetramers, and  
781 higher order oligomers of mini-tetramers, respectively. All the fluorescence intensity  
782 measurements to assign cluster size to an kMBX or kMBXt molecule were performed only in the  
783 first frame for each data set, thereby significantly reducing the possibility of photobleaching  
784 effects.

785

### 786 **Single molecule analyses of Human kinesin-5 (hMBX and hMBXt) mini-tetramers:**

787

788 Image series were drift corrected using the MT images with the Image Stabilizer plug-in for  
789 ImageJ. The output coefficients were then applied to the motor images using the Image  
790 Stabilizer Log Applier plug-in. These transformation coefficients were saved and used for later  
791 steps in the analysis. For images presented in the text, the MT channel was bleach corrected  
792 using the Histogram Matching algorithm in ImageJ.

793 Single molecule tracking was performed on the original, unprocessed images using the  
794 TrackMate (Schindelin et al., 2012; Tinevez et al., 2017) plug-in for ImageJ. Briefly, sub-pixel  
795 localization was performed using a Laplacian of Gaussian (LoG) filter with an estimated spot  
796 diameter of  $0.4\mu\text{m}$  to detect motors. Spots detected in sequential frames were then linked using  
797 the Linear Assignment Problem (LAP) tracker using a maximum displacement of  $0.6\mu\text{m}$ ,  
798 allowing for a two-frame absence of spots, and not permitting track merging or splitting. No  
799 filtering of the detected spots or tracks was done in ImageJ.

800 Quantitative analysis of motor motility activities was performed as follows: MTs were manually  
801 traced out in ImageJ, and the x, y coordinates of these ROIs were saved and imported into  
802 MATLAB. Detected trajectories >3 frames were then projected along the axis of their respective  
803 MT for run length and velocity analysis. Trajectories with a total run length <150nm were not  
804 included in the analysis to filter out statically-bound motors (e.g., those adsorbed on the coverslip  
805 near a MT). All trajectories within 600nm of another MT, or within 600nm of either end of the MT,  
806 were ignored in the analysis of pausing/motility. The local  $\alpha$ -value analysis was performed on all  
807 trajectories with >10 frames using drift-corrected (but not projected) x, y localizations. These  
808 were linearly interpolated to account for the slightly varying frame rate.  $\alpha$ -values were calculated  
809 in sequential 8-frame windows using delays of 2, 3, and 4 frames. Change points were detected  
810 in the resulting  $\alpha$ -values using the findchangepts function in MATLAB (The MathWorks; Natick  
811 MA) with a minimum improvement in the residual error of 0.3 and a minimum distance between  
812 consecutive change points of 3 frames. The means between detected change points were then  
813 evaluated and sections with a mean  $\alpha$ -value >1.1 were deemed processive. The localizations in  
814 the original trajectory were then assigned as processive or paused based on the classification of  
815 the interpolated frame that was nearest to them in time. Subsequent analysis of intensities,  
816 velocities, and inter-pause run lengths was performed using these classifications. Fitting was  
817 done using maximum likelihood estimation (MLE). For the velocity histograms, normal  
818 distributions were fit using the central 96% of the data. For pause time estimates, distributions  
819 were fit using the lower 95% of the data because of the presence of a small number of inactive  
820 motors that are classified to have long “pauses”. For analysis of trajectories in the presence of  
821 AMP-PNP, no minimum run length was used, and the  $\alpha$ -value histogram was fit to the upper  
822 95% of the data to ignore the skew.

823 MT plus-End motor localization intensity analyses were performed as follows: The duration of  
824 time motors/clusters were present at the plus-ends of MTs was quantified using ImageJ. Briefly,  
825 all unobstructed MT plus-ends (identified based on the direction of motor motility) were marked  
826 using point regions of interest (ROIs), which were added to the ROI Manager. These were then  
827 converted to circular ROIs with a diameter of 7 pixels centered on the point using a custom-  
828 written script. The intensity in these ROIs was traced over time using Multi Measure, ensuring  
829 that the recorded measurements included standard deviation, min & max gray value, center of  
830 mass, integrated density, and mean gray value. This process was also repeated for 9  
831 background spots spread throughout the field of view. The output from each movie was saved,  
832 and all data were imported into MATLAB for further analysis. A moving average was applied to  
833 the raw integrated density signal (IDS). In every ROI, a cluster/motor was deemed present in a  
834 given frame of the movie if this filtered IDS in the ROI exceeded that of background ROIs by 3  
835 standard deviations. Only cluster lifetimes >9 frames were considered based on the approximate  
836 time taken for a motor to walk through the ROI. The lifetimes of any clusters present in the first  
837 or last frame of the movie were marked as censored for the subsequent lifetime analysis.  
838 Lifetime analysis was performed by fitting the empirical cumulative distribution function (CDF) to  
839 a mixture of two Weibull CDFs using MLE, taking censoring into account.

#### 841 **Reconstitution of full length and mini-tetramer Kinesin-5 MT crosslinking and sliding**

842  
843 MTs for surface-immobilization were generated via mixture of HiLyte 647 tubulin (TL670M),  
844 biotinylated tubulin (T333P), and unmodified tubulin (T240) at a ratio of 1:1:20 along with 1mM  
845 GMPCPP. MTs were polymerized at 37°C for 1 hour before clarification and stabilization in  
846 30uM Taxol following published protocols (Shimamoto et al, 2015). ‘Free’ MTs for gliding were  
847 generated via mixture of rhodamine tubulin (TL590M) and unmodified tubulin at a ratio of 1:20  
848 along with 1mM GMPCPP, and were polymerized, clarified, and stabilized in 30uM Taxol  
849 following similar protocols.

850 The flow chamber design and assay preparation were modified from a previously described  
851 protocol (Shimamoto et al., 2015). Anti-parallel MT bundles were constructed using passivated

852 glass coverslips coated with SVA-PEG at a ratio of 50 PEG:1 biotin-PEG. All reagents were  
853 prepared with 1X BRB80 buffer. Following each reagent flow-in and incubation, a flush with ~3  
854 chamber volumes of BRB80 was performed. Reagents were introduced stepwise with the  
855 following order and incubation times: (1) 0.5 mg/mL neutravidin, 2 minutes; (2) 0.5 mg/mL alpha  
856 casein surface block, 3 minutes; (3) HiLyte-647 biotinylated MTs with 0.2mg/mL alpha casein  
857 with no additional incubation and immediate flush; (4) kinesin-5 construct at desired final  
858 concentration as reported with 0.2 mg/mL alpha casein, 2 minutes; (5) Rhodamine 561 MTs with  
859 0.2 mg/mL alpha casein, 5 minutes, and the corresponding chamber flush included 1 mM TCEP  
860 bond breaker solution in BRB80; (6) imaging buffer (25 mM HEPES, 25–150 mM KCl, pH 7.5, 10  
861 mM beta-mercapoethanol; 1% glycerol, 0.5% Pluronic-F127, 0.3 mg/ml casein, 3 mM BME, 4  
862 mM ATP-MgCl<sub>2</sub>) with Oxygen Scavenging System (4.5 mg/ml glucose, 350 U/ml glucose  
863 oxidase, 34 U/ml catalase, 1 mM DTT) was then used to flush any unattached MTs. The  
864 chamber was then sealed with clear nail polish prior to experiments.  
865 MT bundles were imaged using three-channel TIRF microscopy using the following exposure  
866 times and laser lines from a Nikon LUNA four-channel laser launch module: HiLyte-647 MTs:  
867 640 nm laser (60% power, 200 ms exposure); GFP-tagged kinesin-5: 488 nm laser (30% power,  
868 100 ms exposure); and rhodamine MTs: 561 nm laser (30% power, 100 ms exposure). Imaging  
869 was performed on a Nikon Ti-E inverted microscope with a CFI Apo 100X/1.49NA oil immersion  
870 TIRF objective. Images were acquired using a Photometric Prime 95B camera controlled with  
871 Nikon NIS Elements software. Analysis of fluorescent data and generation of intensity linescan  
872 data sets were performed using FIJI (ImageJ) tools(Schindelin et al., 2012).  
873  
874  
875

876 **Figure Legends**

877  
878 **Figure 1: The x-ray structure of the kinesin-5 BASS-XL minifilament reveals rigid dimeric**  
879 **coiled-coils emerge from a tetramer core and allow designing kinesin-5 mini-tetramers**  
880

- 881 A) Top, a side views of 34 nm long KLP61F BASS-XL minifilament crystal structure reveals  
882 the formation of dimeric coiled-coils (cyan: 40-nm long) that are rigidly attached to the  
883 BASS tetrameric core (red) and stabilized by the C-terminal extension (dark Blue).  
884 Bottom panel, 90°rotated view compared to top panel.
- 885 B) Top sequence alignment reveals the conservation, and the heptad repeat pattern of the  
886 dimeric coiled-coil (marked in a and d residues), mapped based on the x-ray BASS-XL  
887 structure.  
888 Bottom, view of the dimeric coiled-coil heptad interactions marked in B on the structural  
889 interface shown in A
- 890 C) Domain organization of the designer Kinesin-5 mini-tetramers. The Motor and neck linker  
891 (residues 1-369; Blue) are fused to 20 residue N-terminal coiled-coils (green) and then  
892 fused to the N-terminal dimeric-coiled coil junctions (cyan) of the BASS-XL and the  
893 tetramer core (red) followed by the C-terminal extension (deep blue). The mini-tetramers  
894 may either include or lack the Kinesin-5 C-terminal tail domain (orange).
- 895 D) The structural organization of the designed 38-nm long kinesin-5 mini-tetrameric motor  
896 based on the fusion of domains based on matching the heptad repeats with neck helical  
897 coiled-coil. The tail domains extend near the motor domains of the subunits folded in  
898 anti-parallel orientations.
- 899 E) Scaled-comparison of the mini-tetramer kinesin-5 motors (38 nm), shown on the top,  
900 reveals that they are half the length of the native kinesin-5 tetrameric motors (80 nm),  
901 shown on the bottom.

902  
903 **Figure 2: Kinesin-5 mini-tetramers undergo processive motility interrupted by static**  
904 **pauses along MTs *in vitro*.**  
905

- 906 A) Top, kMBX domain organization. Motor and neck linker domains (1-365, blue) extended  
907 coiled-coil (green), BASS-XL minifilament with its dimerized zone (orange), tetrameric  
908 zone (red) and C-terminal zone (cyan). Middle, structural model for the kMBX mini-  
909 tetramer as shown in Figure 1D.
- 910 B) Top, TIRF microscopy reconstitution setup to examine kMBX motors motility along MTs.  
911 Middle panel, Image of individual MT (red) with kMBX motors moving along toward Mt  
912 plus ends (right side). Bottom panel, Kymograph of above image with kMBX motor  
913 motility along MTs revealing their processive motility with extended pauses (arrows) and  
914 lack of accumulation at MT plus ends.
- 915 C) Top, kMBX domain organization. Motor and neck linker domains (1-365, orange)  
916 extended coiled-coil (green), BASS-XL minifilament with its dimerized zone (cyan),  
917 tetrameric zone (red), C-terminal zone (blue) and C-terminal tail domain (pink). Middle,  
918 structural model for the kMBX mini-tetramer as shown in Figure 1D.
- 919 D) Top, TIRF microscopy setup for kMBXt MT motility assays. Middle panel, Images of  
920 individual MTs (red) with kMBXt motors (green) moving along with MT plus end to the  
921 right. Bottom panel, kymograph of above image with kMBXt motor motility along MTs  
922 revealing their extended pausing and clustering (marked by arrows) and accumulating  
923 kMBXt motor at MT plus ends.
- 924 E) The hMBX-TMR mini-tetramer consists of the human Eg5 motor-neck linker domain (1-  
925 374, orange), the *Drosophila* BASS domain (597-799) with its extended coiled-coil  
926 (green), with its dimerized zone (cyan), tetrameric zone (red), C-terminal zone (blue).

- 927 F) Kymographs of hMBX mini-tetramer motor show that undergo processive motility towards  
928 MT plus-ends and pause infrequently.
- 929 G) The hMBXt-TMR mini-tetramer consists of the human Eg5 motor-neck linker domain (1-  
930 374, orange), the *Drosophila* BASS-XL minifilament (597-799) with its extended coiled-  
931 coil (green), with its dimerized zone (cyan), tetrameric zone (red), C-terminal zone (blue)  
932 and the human Eg5 C-terminal tail domain (913-1056, pink).
- 933 H) An example of a very long run observed for hMBXt motors are shown. 20 frames between  
934 time points. Kymographs for motors showing the presence of pauses between periods of  
935 processive motility. The start (red) and end (blue) points of pauses are identified.
- 936 I) Histogram distributions for motility velocity ( $\mu\text{m/s}$ ) of the kMBX (green), kMBXt (pink),  
937 hMBX (green) and hMBXt (pink) motors along MTs showing that the kMBXt or hMBXt  
938 undergo slower motility than the kMBX and hMBX motors.
- 939 J) Histogram distributions for motility run lengths ( $\mu\text{m}$ ) the kMBX (green), kMBXt (pink),  
940 hMBX (green) and hMBXt (pink) motors along MTs revealing that the kMBXt or hMBXt  
941 motors are generally more processive than the hMBX and kMBX motors.  
942

943 **Figure 3. The Kinesin-5 tail domain induces pauses, increases run lengths and decreases**  
944 **motility velocities of the mini-tetramer kinesin-5.**

- 945
- 946 A) Pauses (red) and periods of processive motility for hMBX motor (blue) were identified in  
947 trajectories based on the slope of the mean-squared displacement ( $\alpha$ ) calculated within a  
948 sliding window along the trajectory.  $\alpha$  fluctuates between  $\sim 2$  and  $\sim 0$  indicating  
949 processive and stationary motility (bottom).
- 950 B) The MSD for the entire trajectories of hMBX motors were fit to an expression that  
951 describes periods of stationary pauses and motile events consisting of processive and  
952 diffusive movements,  $\text{MSD} = (\phi vt)^2 + \phi 2Dt + 2\epsilon^2$  where  $\phi$  is the fraction of time in a motile  
953 state. hMBX motors pause more frequently.
- 954 C) Plotting all local  $\alpha$ -values reveals primarily processive motility (green), while hMBXt  
955 exhibits a bimodal distribution with peaks consistent with static binding ( $\mu 1$ ) and  
956 processive motility ( $\mu 2$ ) (purple).
- 957 D) Histograms showing the frame-to-frame velocity of hMBXt motors (purple; solid line) and  
958 hMBX motors (green; dotted line). hMBX motors move faster than hMBXt motors during  
959 the processive sections of trajectories. Velocities are similar during paused sections. (E)  
960 The total run length for hMBX motors was fit with a single exponential distribution with  
961 mean  $\mu$ . All trajectories  $> 3$  frames were included ( $n = 2056$  trajectories). Unless  
962 otherwise specified,  $n = 111$  trajectories from 3 independent experiments for hMBX  
963 constructs and  $n = 143$  trajectories from 9 independent experiments for hMBXt  
964 constructs.  
965

966 **Figure 4: Kinesin-5 mini-tetramers with the tail domain, but not those without the tail,**  
967 **form multi-motor clusters while undergoing motility along a MT.**

- 968
- 969 A) Mini-tetramers with the tail form clusters while moving along the MT. Two such examples  
970 are shown. Often, one of the motors involved is paused (yellow arrow), a processively  
971 moving motor joins it (orange arrow), and the two continue moving together (orange  
972 arrow). 6 (left) or 10 (right) frames between time points. Scale bars  $1\mu\text{m}$  wide.
- 973 B) Kymographs showing the formation of clusters. Note that many of these cluster's form  
974 while one of the motors involved is paused (red triangles). Scale bars 10s wide and  $1\mu\text{m}$   
975 tall.
- 976 C) The cumulative frequencies and their average for kMBX (green) and kMBXt (pink) motors  
977 to merge into clusters in relationship to the salt concentration (mM) conditions. The  
978 extended data for kMBX and kMBXt motor clustering are shown in figure supplement.

- 979 D, E, F) Intensity distribution for constructs (D) with the tail domain in the presence of ATP,  
980 (E) with the tail domain in the presence of AMP-PNP, and (F) without the tail domain in  
981 the presence of ATP, suggesting that the mini-tetramers require the tail domain and  
982 motility in order to form clusters. Clusters likely correspond to 2-3 motors, and the  
983 blurring of the intensity distribution for motors in the presence of ATP is likely due to the  
984 quenching and unquenching of the TMR sensors used as labels during motor stepping.  
985 Lines are ~6500au apart. For D, n = 1406 trajectories from 9 independent experiments.  
986 For E, n = 1298 trajectories from 2 independent experiments. For F, n = 2056 trajectories  
987 from 3 independent experiments.
- 988 G) Total run length distributions for single motors (light purple; dotted line) and clusters (dark  
989 purple; solid line), both with the tail. Distributions were fit with a double exponential  
990 distribution, and both groups have a short ( $\mu_1$ ) and long ( $\mu_2$ ) run length population.  
991 However, the fraction of motors in the long run length population ( $p_2$ ) is larger for  
992 clusters.
- 993 H, I) Motors often reach the plus-ends of stabilized MTs and remain bound there for some  
994 time. Lifetimes were fit to a Weibull distribution. The hMBXt motors were best fit by a  
995 double Weibull distribution, suggesting the presence of populations with a short and long  
996 lifetime. The short lifetime ( $\tau_1$ ) was similar for both constructs, whereas the long lifetime  
997 ( $\tau_2$ ) was longer for hMBXt than hMBX motors. The fraction of the population with a short  
998 lifetime ( $p_1$ ) was also higher for hMBX motors, agreeing with the observation that hMBX  
999 motors do not form clusters along the length of the MT.
- 1000 J) Distribution of lifetimes of motors/clusters at the ends of MTs as a function of their starting  
1001 intensity (average intensity of the first 5 frames they are detected). hMBX motors (green)  
1002 generally arrive as single motors, whereas hMBXt motors (purple) often arrive as  
1003 clusters. Open circles denote censored lifetimes (present in first or last frame of movie,  
1004 indicating they are at least as long or longer than the point plotted).
- 1005 K) The cumulative MT plus-end association times for kMBX and kMBXt motors and their  
1006 average values in relationship to the salt concentration (mM). The extended data for  
1007 kMBX and kMBXt motor clustering are shown in Figure 4 figure supplement 2-3.

1009 **Figure 5: Kinesin-5 mini-tetramers show defects in crosslinking MTs but enhanced MT**  
1010 **sliding once aligned, compared to native kinesin-5.**

- 1011
- 1012 A) Representative TIRF images of surface-immobilized MTs (magenta) crosslinked via  
1013 kinesin-5 (green) constructs to free MTs (red). Four different kinesin-5 constructs were  
1014 examined: hFLt, hFL, kMBXt, and kMBX. Scale bar = 10 microns.
- 1015 B) Percentage of surface-immobilized MTs that engaged in kinesin-5 mediated crosslinking  
1016 with free MTs for each kinesin-5 construct. N=8 fields of view analyzed per condition.
- 1017 C) Sample MT pairs (top) and kymographs (bottom) depicting MT sliding driven by either  
1018 hFLt (left) or kMBXt (right). Free MT (red) and kinesin-5-GFP or nNG (green) are shown.  
1019 Pauses are identified by vertical yellow bar. Scale bar = 4 microns; frame rate for hFLt =  
1020 10 seconds per frame; for kMBXt = 5 seconds per frame.
- 1021 D) Number of pauses or velocity reduction events observed per micron for hFLt and kMBXt  
1022 driven MT sliding. N = 11 events for hFLt, N = 9 events for kMBXt.
- 1023 E) Average MT sliding rate calculated for bundles at different ATP concentrations. N = 6  
1024 events for each condition. Error bars are S.D. Values are reported in Table 3.

1025

1026 **Figure 6: Kinesin-5 tail to motor regulation and minifilament length modulate motor**  
1027 **clustering and features of MT-sliding motility.**

1028

- 1029 A) The Kinesin-5 mini-tetramers are 38 nm in length leading to a decrease in torsional  
1030 flexibility compared to native kinesin-5, which are 80 nm in length and have higher  
1031 torsional flexibility.
- 1032 B) Top panel, kinesin-5 mini-tetramers without the tail domain show processive motility  
1033 punctuated by pauses and little residence at MT-plus ends. Bottom panel, kinesin-5 mini-  
1034 tetramers with the tail domain show increased pausing, coupled with motor clustering  
1035 mediated by cross motor-tail interactions between mini-tetramers.
- 1036 C) MT sliding motility mediated by native kinesin-5 leads to 80-nm separation between  
1037 paired MTs, which are slide apart with normal sliding velocity, which is punctuated by  
1038 pauses and is lower than twice motility velocity of each motor end along each MT.
- 1039 D) MT sliding motility by the kinesin-5 mini-tetramers leads to 38-nm separation between the  
1040 paired MTs and a more efficient MT sliding motility that approaches closely to twice the  
1041 motility velocity of each motor end.
- 1042 E) The native kinesin-5 motor MT pair alignment is efficient due to torsional flexibility of the  
1043 minifilament
- 1044 F) Kinesin-5 mini-tetramer MT pair alignment is poor due to decreased torsional flexibility of  
1045 its shortened minifilament.
- 1046  
1047  
1048  
1049  
1050

1051  
1052

Table 1. X-ray crystallographic Data collection and refinement statistics.

	BASS-XL
<b>Data collection</b>	
Resolution range	126.55- 4.40 (4.64 - 4.40)
Wavelength (Å)	0.979
Space group	C 2
Unit cell (Å): <i>a</i> , <i>b</i> , <i>c</i>	253.18, 84.89, 96.77
(°): β	91.44
Total number of observed reflections	55597 (7964)
Unique reflections	13060 {10508}†
Average mosaicity	0.33
Multiplicity	4.3 (4.3)
Completeness (%)	98.7 (98.8) {79.76}†
Mean <i>I</i> /σ( <i>I</i> )	4.6 (1.8)
Wilson B-factor	38.14
<i>R</i> <sub>merge</sub> <sup>a</sup>	0.10 (0.47)
<b>Structure refinement</b>	
<i>R</i> <sub>work</sub>	0.274 (0.251)
<i>R</i> <sub>free</sub>	0.310 (0.368)
Molecules per asymmetric unit	4
Number of non-hydrogen atoms	5037
macromolecules	5037
Solvent	0
Protein residues	702
RMS bond lengths (Å)	0.002
RMS bond angles (°)	0.56
Ramachandran favored (%)	96.2
Ramachandran allowed (%)	3.6
Ramachandran outliers (%)	0.43
Rotamer outliers (%)	0.41
Clashscore	11.42
Mean <i>B</i> values (Å <sup>2</sup> )	
Overall	113.93
macromolecules	113.93
Number of TLS groups	11

Parenteses numbers represent the highest-resolution shell.

†Numbers represent the truncated data after treated with ellipsoidal truncation and anisotropic scaling.

$$^a R_{\text{merge}} = \frac{\sum_{hkl} \sum_i |I_i(hkl) - I_{\text{av}}(hkl)|}{\sum_{hkl} \sum_i I_i(hkl)}$$

1053  
1054  
1055  
1056



1057 Table 2: *Drosophila* Kinesin-5 mini-tetramer motor motility properties

1058

<b>kMBX</b>	<b>Velocity (nm/s)</b>	<b>Run length (nm)</b>	<b>Run time (s)</b>	<b>Merging freq (<math>\mu\text{m}^{-1}\text{min}^{-1}</math>)</b>	<b>MT plus-end dwell time(s)</b>
25 mM KCl	115 ± 3 n=340	N/A	N/A	N/A	N/A
50 mM KCl	144 ± 6 n=136	1014±222	9±1	0.006±0.001	78±19
100 mM KCl	156 ± 8 n =66	2137±428	16±4	0.001±0.0007	25±18
<b>kMBXt</b>					
25 mM KCl	78 ± 4 n=52	3832±433	56 ± 8	0.007 ± 0.002	125±51
50 mM KCl	127 ± 4 n=136	3135±222	29 ± 1	0.011 ± 0.002	117±15
100 mM KCl	114 ± 5 n=88	5060±605	51 ± 7	0.050 ± 0.008	267±45
125 mM KCl	136 ± 4 n=149	5440±362	45 ± 4	0.023 ± 0.006	147±34
150 mM KCl	119 ± 6 n=19	3347±538	29 ± 5	0.001 ± 0.0008	25±17

1059

1060

1061 Table 3: MT sliding velocities for Native and mini-tetramer kinesin-5 motors

1062

ATP ( $\mu\text{M}$ )	hFLt	kMBXt
10	N/A	23 +/- 11 nm/s (n=9)
25	N/A	35 +/- 15 nm/s (n=6)
50	N/A	51 +/- 12 nm/s (n=11)
100	69 +/- 11 nm/s (n=13)	82 +/- 17 nm/s (n=15)
250	91 +/- 14 nm/s (n=17)	103 +/- 21 nm/s (n=14)

1063

1064

1065

1066 **Figure Legends for figure supplements**

1067  
1068 **Figure 1 figure supplement 1. Details of the BASS-XL x-ray crystal structure**  
1069 **determination.**

- 1070  
1071 A) Purification and Crystallization of the BASS-XL protein: left panel, Size Exclusion  
1072 Chromatography (SEC) trace showing the purified BASS-XL. Middle panel, SDS-PAGE  
1073 of purified BASS-XL. Right panel, images of BASS-XL C2 crystals used for x-ray  
1074 structure determination.  
1075 B) Alignment of the BASS (grey) and BASS-XL (red) N-terminal structure ends reveal the  
1076 extension of the BASS-XL and formation of the heptad repeats at the N-terminal end.  
1077 C) 2Fo-Fc map revealing the final model for BASS-XL built using the BASS-XL  
1078 crystallographic data at 4.4-Å resolution. The model reveals the detailed helical coiled-  
1079 coil dimers at the BASS-XL N-terminal end.  
1080 D) Crystallographic packing organization of BASS-XL minifilaments within the C2 space  
1081 group for crystals used for structure determination.  
1082

1083 **Figure 1 figure supplement 2. Designing kinesin-5 mini-tetramers using the BASS-XL x-**  
1084 **ray structure as a short mini-filament template.**

- 1085 A) Domain organization of designer Drosophila kinesin-5 mini-tetramers. KLP61F motor and  
1086 neck linker domain (orange: residues 1-369) were fused to an extended BASS-XL  
1087 minifilament, with its coiled-coil extension (green), dimerized region (cyan), tetrameric region  
1088 (red) and C-terminal stabilizing zone (blue). The kMBXt construct included fusing the C-  
1089 terminal kinesin-5 tail domain (residues 910-1036) to the C-terminal domain of the BASS-XL  
1090 minifilament.  
1091 B) SEC-trace and SDS-PAGE for a peak fraction of the bacterially expressed of the C-terminally  
1092 neon green (mNG) tagged KMBX and kMBXt motors.  
1093 C) Top, a side view of a structural model revealing the organization of the designed bipolar mini-  
1094 tetrameric kinesin-5 motor with various regions (colored as described A) shown. The model  
1095 reveals the motor neck-linker domains are oriented to face in different directions due to their  
1096 positioning on the BASS-XL minifilament and the mini-tetrameric motor is 38-nm in length,  
1097 which is roughly half the length of native kinesin-5. Below, a 90° rotated view of the view  
1098 shown on top. D) a subunit colored view of the kinesin-5 mini-tetrameric motor design  
1099 revealing the subunit organization of the motor and minifilament domains. Below, a 90°  
1100 rotated view of the view shown on top.  
1101

1102 **Figure 3-figure supplement 1.**

- 1103  
1104 A) Additional traces of parsing analysis for trajectories of hMBXt, similar to Figure 1d. Pauses  
1105 (red) and periods of processive motility (blue) were identified in trajectories (top plots) based  
1106 on the local  $\alpha$ -value calculated within a sliding window along the trajectory, which fluctuated  
1107 between  $\sim 2$  and  $\sim 0$  (bottom plots).  
1108 B) Histograms showing the number of distinct sections identified as paused for hMBXt motors  
1109 (purple) and hMBX motors (green) in a given trajectory as a fraction of the number of long  
1110 trajectories ( $n = 143$  for hMBXt and  $n = 111$  for hMBX).  
1111 C) the number of all trajectories  $>3$  frames ( $n = 1406$  for hMBXt motors and  $n = 2056$  for hMBX).  
1112 This shows that fewer of the trajectories for hMBX motors were long enough to use in our  
1113 parsing analysis and, as short trajectories were less likely to contain pauses (see, for example  
1114 Figure 2C), shows that a small fraction of total trajectories contained pauses for hMBX  
1115 motors.  
1116 D, E) MSD curves for paused (red) and processive (blue) sections for hMBXt (D) and hMBX (E)  
1117 motors plotted on a linear scale, revealing the parabolic shape characteristic of super-

1118 diffusive motility for processive sections, and a horizontal line for paused sections. Lines were  
1119 fit to  $\langle x^2 \rangle = (v^2 + \sigma_v^2)\tau^2 + 2\varepsilon^2$  and  $\langle x^2 \rangle = 2\varepsilon^2$ , respectively. Error bars represent SEM. For a, n =  
1120 143 trajectories from 9 independent experiments. For b, n = 111 trajectories from 3  
1121 independent experiments.

1122 **F)** Kymograph showing the static binding of mini-tetramers in the presence of AMP-PNP. Scale  
1123 bar 10s wide and 1 $\mu$ m tall.

1124 **G)** Repeating the local  $\alpha$ -value analysis for mini-tetramers with the tail domain in the presence of  
1125 AMP-PNP (black; dotted line) reveals a uni-modal distribution, similar to the mean  $\alpha$ -value of  
1126 the paused sections (red; solid line) in the presence of ATP. In contrast, the mean  $\alpha$ -value of  
1127 processive sections (blue; solid line) in the presence of ATP is closer to 2. For AMP-PNP, n =  
1128 442 trajectories from 2 independent experiments. For ATP, n = 143 trajectories from 9  
1129 independent experiments.

1130  
1131 **Figure 4-figure supplement 1.** Measuring kMBXt clustering using tracking and intensity  
1132 analysis.

1133  
1134 **A)** Low magnification view of the MT (left) and kMBXt (right field) prior to analysis.  
1135 **B)** The intensity analysis (right) for all spots detected (left) identified via TrackMate plugin using  
1136 FIJI/imageJ. The kMBXt intensity histogram is presented was converted into cluster values  
1137 based on the fluorescence intensity of NG per motor subunit within each mini-tetramer.  
1138 Details are described in materials and methods.

1139  
1140 **Figure 4 figure supplement 2: Example kymographs for kMBXt clustering at increasing**  
1141 **ionic strengths**

1142  
1143 Example kymographs of kMBXt clustering along MTs at (A) 25 mM, (B) 50 mM, (C) 100 mM,  
1144 (D) 125 mM KCl and (E) 150 mM KCl conditions. The kymographs show that clustering  
1145 increases dramatically from 25 to 100 mM KCl but it decreases at 125 and 150 mM KCl. The  
1146 MT plus-end accumulation seems to concentrate the largest kMBX clusters (left side of each  
1147 kymograph). (F) Description for types of cluster and motor merging events described in Figure  
1148 4 figure supplement 4B.

1149  
1150 **Figure 4-figure supplement 3:** Characterizing kMBXt motility properties in relation cluster  
1151 formation. Distribution for motility velocity A), Run length. B) and Run time. C) for kMBX  
1152 (green) and kMBXt (purple) at 25-150 mM KCl. The types of clusters formed for kMBXt at  
1153 different conditions. For each type a smaller intensity spot merges with larger intensity spot  
1154 (i.e., 1+2). These intensities were delineated using the approach presented in Figure 4 figure  
1155 supplement 1 and described in materials and methods. D) Relationship of kMBXt motility  
1156 velocity (left), Run length (middle) and run time(right) to cluster size for the 25 mM (green), 50  
1157 mM (pink), 100 mM (Gray), 125 mM (Cyan) and 150 mM KCl (orange). These data show that  
1158 cluster size does not correlate to any of the properties described.

1159  
1160 **Figure 4 figure supplement 4: Analyses of MT plus-end accumulation of kinesin-5 mini-**  
1161 **tetramers**

1162  
1163 **A)** Clusters, which generally arrive at plus-ends as assemblies and dissociate as assemblies,  
1164 were detected based on the intensity in a ROI over time. Blue line denotes intensity trace in  
1165 ROI at the plus-end of a MT. Magenta spots identify frames in which no motor is identified as  
1166 present. Green spots identify frames in which motor is identified as present. Other thin lines  
1167 denote intensity traces of background ROIs used as a reference to identify the presence of a  
1168 motor. Inset: An example of a motor arriving and falling off a plus-end is shown. 20 frames  
1169 between time points. Scale bar 1 $\mu$ m wide.

- 1170 **B)** Histograms of the frame-to-frame velocities for single motors (light purple; dotted line) and  
1171 clusters (dark purple; solid line). During the processive sections of trajectories, clusters move  
1172 more slowly than single motors. Their velocities during paused sections are similar. For a and  
1173 e,  $n = 143$  trajectories from 9 independent experiments for hMBXt and  $n = 111$  trajectories  
1174 from 3 independent experiments for hMBX. For b and c,  $n = 351$  plus-end clusters detected  
1175 from 8 independent experiments for hMBXt motors and  $n = 211$  plus-end clusters detected  
1176 from 3 independent experiments for hMBX motors.
- 1177 **C)** Additional traces of cluster detection at the plus-ends of MTs, similar to Figure 4C. Clusters  
1178 generally arrive at plus-ends as a whole and dissociate as a whole, regardless of the plateau  
1179 intensity, but we did observe single motors appearing to join a pre-existing cluster, as well as  
1180 some clusters forming at the plus-end (e.g., top left). Blue line denotes intensity trace in ROI  
1181 at the plus-end of a MT. Magenta spots identify frames in which no motor is identified as  
1182 present. Green spots identify frames in which motor is identified as present. Other thin lines  
1183 denote intensity traces of background ROIs used as a reference to identify the presence of a  
1184 motor. Top four traces for hMBXt motors and lower two for hMBX motors.
- 1185 **D)** The cumulative distribution function for the mixed Weibull distribution used to fit the empirical  
1186 cumulative distribution of lifetimes for hMBX and hMBXt motors, as well as the obtained  
1187 estimates of the parameters. Note that the short lifetimes and shape parameters are similar,  
1188 while the longer lifetime is longer for hMBXt motors. Notably, the weighting of the shorter  
1189 lifetime is also lower for hMBXt motors, suggesting that a larger fraction of motors is in the  
1190 longer lifetime population.
- 1191 **E)** An example of a cluster of human kinesin-5 HMBXt motors dragging the plus-end at which the  
1192 motors accumulated along another MT, acting to align the two MTs. This demonstrates that  
1193 the plus-end clusters are still motile and are able to withstand load (the MTs are quite bent and  
1194 still anchored to the coverslip at some sites by an avidin-biotin interaction). Note that to  
1195 observe this, a higher density of MTs was immobilized using a lower density of Neutraavidin. 50  
1196 frames between time points. Scale bar  $2\mu\text{m}$  wide.

1197  
1198 **Figure 5 figure supplement 1: Analyses of Velocity of MT sliding for native and mini-**  
1199 **tetramer kiensin-5:** Individual frames from time-lapse image series were processed via linescan  
1200 analysis to determine MT minus-end positions. These values are then plotted as a function of  
1201 time for (a) hFLt and (b) kMBXt proteins. Velocities are calculated by applying a sliding window  
1202 function of width 5 frames to the position data and a linear slope is calculated for the  
1203 corresponding data sets (b,d). Velocity values below 15 nm/s for more than 3 consecutive  
1204 frames were then classified as pausing events (red dashed line in b,d).

1205  
1206

1207 **Video Legends**

1208  
1209 **Video 1:** Large-scale view of hMBXt motors (green) undergoing motility along MTs (magenta)  
1210 revealing kinesin-5 mini-tetramer motor pausing, clustering, and MT plus end  
1211 association.

1212  
1213 **Video 2:** Close-view of hMBX motors (green) undergoing motility, forming clusters, with pausing  
1214 and while dwelling at MT (magenta) plus-ends.

1215 **Video 3:** motility of kMBXt motors at four different ionic strength conditions (25-150 mM KCl)  
1216 revealing the impact of ionic strength on motor clustering, processive motility and plus-  
1217 end attachment. Clustering is improved at 50 mM KCl and decreases at 100-150 mM  
1218 KCl. MT plus end accumulation occurs at 25-100 mM KCl and is diminished at 150  
1219 mM KCl.

1220 **Video 4:** An example of a cluster of kinesin-5 hMBXt motors dragging the plus-end at which the  
1221 motors accumulated along another MT, acting to align the two MTs. This demonstrates  
1222 that the plus-end clusters are still motile and are able to withstand load (the MTs are  
1223 quite bent and still anchored to the coverslip at some sites by an avidin-biotin  
1224 interaction). Note that to observe this, a higher density of MTs was immobilized using a  
1225 lower density of Neutravidin. 50 frames between time points. Scale bar 2 $\mu$ m wide.

1226  
1227 **Video 5:** Three examples of MT sliding by native kinesin-5 (hFLt). The hFLt motors (green) slide  
1228 a paired MT (red) along the anchored MT (magenta).

1229  
1230 **Video 6:** Three examples of MT sliding by mini-tetramer-kinesin-5 (kMBXt). The kMBXt motors  
1231 (green) slide a paired MT (red) along the anchored MT (magenta).  
1232

1233 References:

- 1234
- 1235 Acar, S., Carlson, D.B., Budamagunta, M.S., Yarov-Yarovoy, V., Correia, J.J., Ninonuevo, M.R.,  
1236 Jia, W., Tao, L., Leary, J.A., Voss, J.C., *et al.* (2013). The bipolar assembly domain of the mitotic  
1237 motor kinesin-5. *Nat Commun* 4, 1343.
- 1238 Al-Bassam, J. (2014). Reconstituting Dynamic Microtubule Polymerization Regulation by TOG  
1239 Domain Proteins. *Reconstituting the Cytoskeleton* 540, 131-148.
- 1240 Andreasson, J.O.L., Clancy, B.E., Behnke-Parks, W., Rosenfeld, S.S., and Block, S.M. (2012). A  
1241 Universal Pathway for Kinesin Stepping. *Biophys J* 102, 369a-369a.
- 1242 Arcizet, D., Meier, B., Sackmann, E., Radler, J.O., and Heinrich, D. (2008). Temporal Analysis of  
1243 Active and Passive Transport in Living Cells. *Phys Rev Lett* 101.
- 1244 Beausang, J.F., Goldman, Y.E., and Nelson, P.C. (2011). Changeoint Analysis for Single-  
1245 Molecule Polarized Total Internal Reflection Fluorescence Microscopy Experiments. *Method*  
1246 *Enzymol*, 431-463.
- 1247 Bertran, M.T., Sdelci, S., Regue, L., Avruch, J., Caelles, C., and Roig, J. (2011). Nek9 is a Plk1-  
1248 activated kinase that controls early centrosome separation through Nek6/7 and Eg5. *Embo*  
1249 *Journal* 30, 2634-2647.
- 1250 Blangy, A., Lane, H.A., d'Herin, P., Harper, M., Kress, M., and Nigg, E.A. (1995).  
1251 Phosphorylation by p34cdc2 regulates spindle association of human Eg5, a kinesin-related  
1252 motor essential for bipolar spindle formation in vivo. *Cell* 83, 1159-1169.
- 1253 Bodrug, T., Wilson-Kubalek, E.M., Nithianantham, S., Thompson, A.F., Alfieri, A., Gaska, I.,  
1254 Major, J., Debs, G., Inagaki, S., Gutierrez, P., *et al.* (2020). The kinesin-5 tail domain directly  
1255 modulates the mechanochemical cycle of the motor domain for anti-parallel microtubule sliding.  
1256 *Elife* 9.
- 1257 Cahu, J., Olichon, A., Hentrich, C., Schek, H., Drinjakovic, J., Zhang, C.J., Doherty-Kirby, A.,  
1258 Lajoie, G., and Surrey, T. (2008). Phosphorylation by Cdk1 Increases the Binding of Eg5 to  
1259 Microtubules In Vitro and in Xenopus Egg Extract Spindles. *Plos One* 3.
- 1260 Castoldi, M., and Popov, A.V. (2003). Purification of brain tubulin through two cycles of  
1261 polymerization-depolymerization in a high-molarity buffer. *Protein Expr Purif* 32, 83-88.
- 1262 Chen, G.Y., Cleary, J.M., Asenjo, A.B., Chen, Y., Mascaro, J.A., Arginteanu, D.F.J., Sosa, H.,  
1263 and Hancock, W.O. (2019). Kinesin-5 Promotes Microtubule Nucleation and Assembly by  
1264 Stabilizing a Lattice-Competent Conformation of Tubulin. *Current Biology* 29, 2259-+.
- 1265 Chen, G.Y., Mickolajczyk, K.J., and Hancock, W.O. (2016). The Kinesin-5 Chemomechanical  
1266 Cycle Is Dominated by a Two-heads-bound State. *Journal of Biological Chemistry* 291, 20283-  
1267 20294.
- 1268 Chen, Y.L., and Hancock, W.O. (2015). Kinesin-5 is a microtubule polymerase. *Nature*  
1269 *Communications* 6.
- 1270 Chugh, M., Reissner, M., Bugiel, M., Lipka, E., Herrmann, A., Roy, B., Muller, S., and Schaffer,  
1271 E. (2018). Phragmoplast Orienting Kinesin 2 Is a Weak Motor Switching between Processive  
1272 and Diffusive Modes. *Biophys J* 115, 375-385.
- 1273 Cross, R.A., and McAinsh, A. (2014). Prime movers: the mechanochemistry of mitotic kinesins.  
1274 *Nat Rev Mol Cell Bio* 15, 257-271.
- 1275 Drosopoulos, K., Tang, C., Chao, W.C.H., and Linardopoulos, S. (2014). APC/C is an essential  
1276 regulator of centrosome clustering. *Nature Communications* 5.
- 1277 Duselder, A., Fridman, V., Thiede, C., Wiesbaum, A., Goldstein, A., Klopfenstein, D.R., Zaitseva,  
1278 O., Janson, M.E., Gheber, L., and Schmidt, C.F. (2015). Deletion of the Tail Domain of the  
1279 Kinesin-5 Cin8 Affects Its Directionality. *J Biol Chem* 290, 16841-16850.
- 1280 Emsley, P., Lohkamp, B., Scott, W.G., and Cowtan, K. (2010). Features and development of  
1281 Coot. *Acta Crystallogr D Biol Crystallogr* 66, 486-501.
- 1282 Falnikar, A., Tole, S., and Baas, P.W. (2011). Kinesin-5, a mitotic microtubule-associated motor  
1283 protein, modulates neuronal migration. *Molecular Biology of the Cell* 22, 1561-1574.

1284 Furuta, K., Furuta, A., Toyoshima, Y.Y., Amino, M., Oiwa, K., and Kojima, H. (2013). Measuring  
1285 collective transport by defined numbers of processive and nonprocessive kinesin motors. *P Natl*  
1286 *Acad Sci USA* *110*, 501-506.

1287 Hafner, A.E., Santen, L., Rieger, H., and Shaebani, M.R. (2016). Run-and-pause dynamics of  
1288 cytoskeletal motor proteins. *Sci Rep-Uk* *6*.

1289 Henty-Ridilla, J.L., Rankova, A., Eskin, J.A., Kenny, K., and Goode, B.L. (2016). Accelerated  
1290 actin filament polymerization from microtubule plus ends. *Science* *352*, 1004-1009.

1291 Hildebrandt, E.R., Gheber, L., Kingsbury, T., and Hoyt, M.A. (2006). Homotetrameric form of  
1292 Cin8p, a *Saccharomyces cerevisiae* kinesin-5 motor, is essential for its in vivo function. *J Biol*  
1293 *Chem* *281*, 26004-26013.

1294 Kapitein, L.C., Peterman, E.J., Kwok, B.H., Kim, J.H., Kapoor, T.M., and Schmidt, C.F. (2005).  
1295 The bipolar mitotic kinesin Eg5 moves on both microtubules that it crosslinks. *Nature* *435*, 114-  
1296 118.

1297 Kashina, A.S., Scholey, J.M., Leszyk, J.D., and Saxton, W.M. (1996). An essential bipolar mitotic  
1298 motor. *Nature* *384*, 225.

1299 Liebschner, D., Afonine, P.V., Baker, M.L., Bunkoczi, G., Chen, V.B., Croll, T.I., Hintze, B.,  
1300 Hung, L.W., Jain, S., McCoy, A.J., *et al.* (2019). Macromolecular structure determination using  
1301 X-rays, neutrons and electrons: recent developments in Phenix. *Acta Crystallogr D* *75*, 861-877.

1302 Lin, S., Liu, M., Son, Y.J., Himes, B.T., Snow, D.M., Yu, W.Q., and Baas, P.W. (2011). Inhibition  
1303 of Kinesin-5, a Microtubule-Based Motor Protein, As a Strategy for Enhancing Regeneration of  
1304 Adult Axons. *Traffic* *12*, 269-286.

1305 McHugh, T., Gluszek, A.A., and Welburn, J.P.I. (2018). Microtubule end tethering of a  
1306 processive kinesin-8 motor Kif18b is required for spindle positioning. *Journal of Cell Biology* *217*,  
1307 2403-2416.

1308 Michalet, X. (2011). Mean Square Displacement Analysis of Single-Particle Trajectories with  
1309 Localization Error. *Biophys J* *100*, 252-252.

1310 Myers, K.A., and Baas, P.W. (2007). Kinesin-5 regulates the growth of the axon by acting as a  
1311 brake on its microtubule array. *Journal of Cell Biology* *178*, 1081-1091.

1312 Nadar, V.C., Ketschek, A., Myers, K.A., Gallo, G., and Baas, P.W. (2008). Kinesin-5 Is Essential  
1313 for Growth-Cone Turning. *Current Biology* *18*, 1972-1977.

1314 Nadar, V.C., Lin, S., and Baas, P.W. (2012). Microtubule Redistribution in Growth Cones Elicited  
1315 by Focal Inactivation of Kinesin-5. *J Neurosci* *32*, 5783-5794.

1316 Pandey, H., Reithmann, E., Goldstein-Levitin, A., Al-Bassam, J., Frey, E., and Gheber, L.  
1317 (2021). Drag-induced directionality switching of kinesin-5 Cin8 revealed by cluster-motility  
1318 analysis. *Sci Adv* *7*.

1319 Rapley, J., Nicolas, M., Groen, A., Regue, L., Bertran, M.T., Caelles, C., Avruch, J., and Roig, J.  
1320 (2008). The NIMA-family kinase Nek6 phosphorylates the kinesin Eg5 at a novel site necessary  
1321 for mitotic spindle formation. *Journal of Cell Science* *121*, 3912-3921.

1322 Rozelle, D.K., Hansen, S.D., and Kaplan, K.B. (2011). Chromosome passenger complexes  
1323 control anaphase duration and spindle elongation via a kinesin-5 brake. *Journal of Cell Biology*  
1324 *193*, 285-294.

1325 Ruthardt, N., Lamb, D.C., and Brauchle, C. (2011). Single-particle Tracking as a Quantitative  
1326 Microscopy-based Approach to Unravel Cell Entry Mechanisms of Viruses and Pharmaceutical  
1327 Nanoparticles. *Mol Ther* *19*, 1199-1211.

1328 Saunders, A.M., Powers, J., Strome, S., and Saxton, W.M. (2007). Kinesin-5 acts as a brake in  
1329 anaphase spindle elongation. *Current Biology* *17*, R453-R454.

1330 Schindelin, J., Arganda-Carreras, I., Frise, E., Kaynig, V., Longair, M., Pietzsch, T., Preibisch,  
1331 S., Rueden, C., Saalfeld, S., Schmid, B., *et al.* (2012). Fiji: an open-source platform for  
1332 biological-image analysis. *Nature Methods* *9*, 676-682.

1333 Scholey, J.E., Nithianantham, S., Scholey, J.M., and Al-Bassam, J. (2014). Structural basis for  
1334 the assembly of the mitotic motor Kinesin-5 into bipolar tetramers. *Elife* *3*, e02217.

1335 Shapira, O., Goldstein, A., Al-Bassam, J., and Gheber, L. (2017). A potential physiological role  
1336 for bi-directional motility and motor clustering of mitotic kinesin-5 Cin8 in yeast mitosis. *J Cell Sci*  
1337 *130*, 725-734.

1338 Shimamoto, Y., Forth, S., and Kapoor, T.M. (2015). Measuring Pushing and Braking Forces  
1339 Generated by Ensembles of Kinesin-5 Crosslinking Two Microtubules. *Dev Cell* *34*, 669-681.

1340 Strong, M., Sawaya, M.R., Wang, S.S., Phillips, M., Cascio, D., and Eisenberg, D. (2006).  
1341 Toward the structural genomics of complexes: Crystal structure of a PE/PPE protein complex  
1342 from *Mycobacterium tuberculosis*. *P Natl Acad Sci USA* *103*, 8060-8065.

1343 Subramanian, R., and Gelles, J. (2007). Two distinct modes of processive kinesin movement in  
1344 mixtures of ATP and AMP-PNP. *J Gen Physiol* *130*, 445-455.

1345 Telley, I.A., Bieling, P., and Surrey, T. (2011). Reconstitution and Quantification of Dynamic  
1346 Microtubule End Tracking In Vitro Using TIRF Microscopy. *Methods Mol Biol* *777*, 127-145.

1347 Tinevez, J.Y., Perry, N., Schindelin, J., Hoopes, G.M., Reynolds, G.D., Laplantine, E., Bednarek,  
1348 S.Y., Shorte, S.L., and Eliceiri, K.W. (2017). TrackMate: An open and extensible platform for  
1349 single-particle tracking. *Methods* *115*, 80-90.

1350 Toprak, E., Yildiz, A., Hoffman, M.T., Rosenfeld, S.S., and Selvin, P.R. (2009). Why kinesin is so  
1351 processive. *P Natl Acad Sci USA* *106*, 12717-12722.

1352 Valentine, M.T., and Block, S.M. (2009). Force and Premature Binding of ADP Can Regulate the  
1353 Processivity of Individual Eg5 Dimers. *Biophys J* *97*, 1671-1677.

1354 Vershinin, M., Carter, B.C., Razafsky, D.S., King, S.J., and Gross, S.P. (2007). Multiple-motor  
1355 based transport and its regulation by Tau. *P Natl Acad Sci USA* *104*, 87-92.

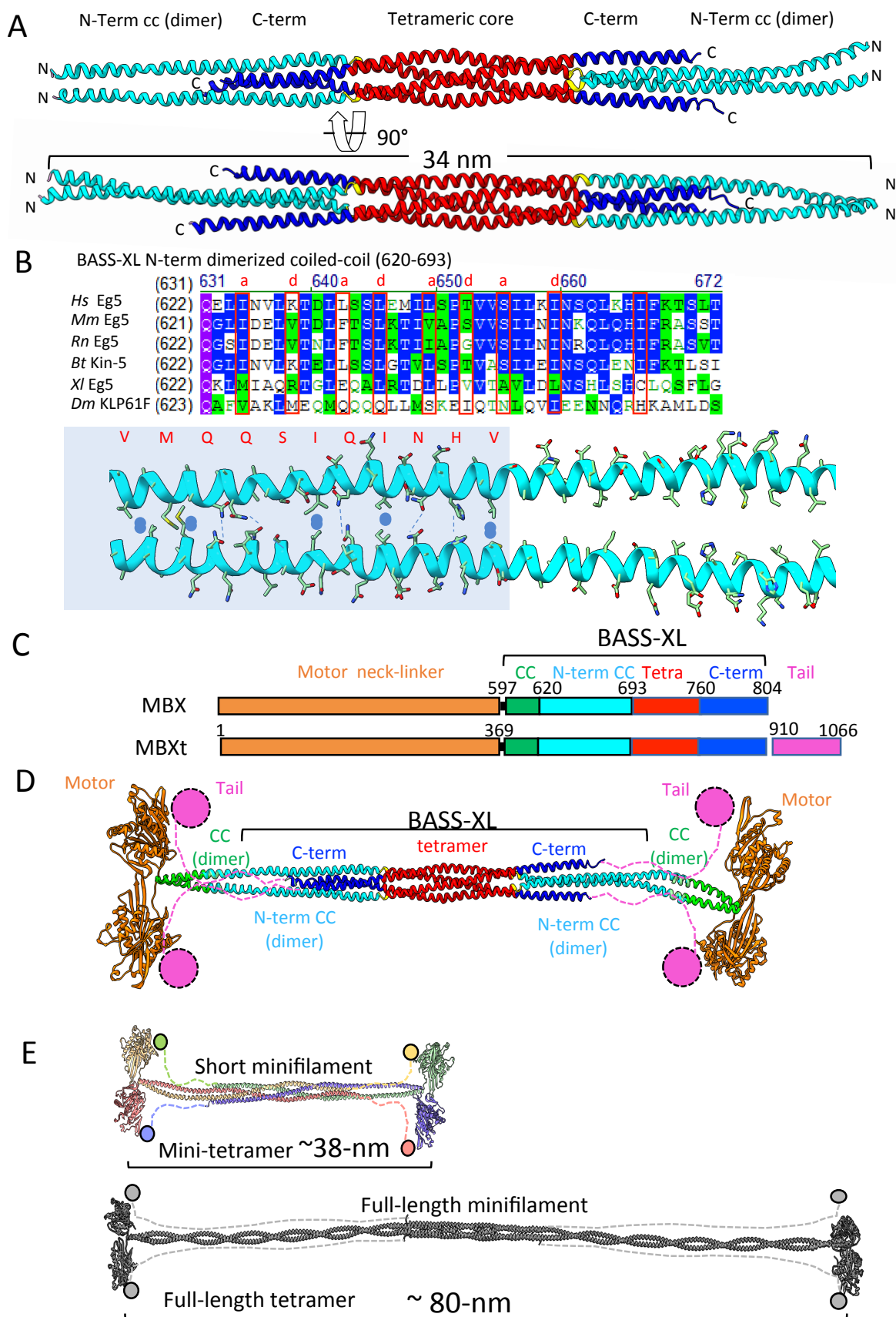
1356 Vugmeyster, Y., Berliner, E., and Gelles, J. (1998). Release of isolated single kinesin molecules  
1357 from microtubules. *Biochemistry-U S A* *37*, 747-757.

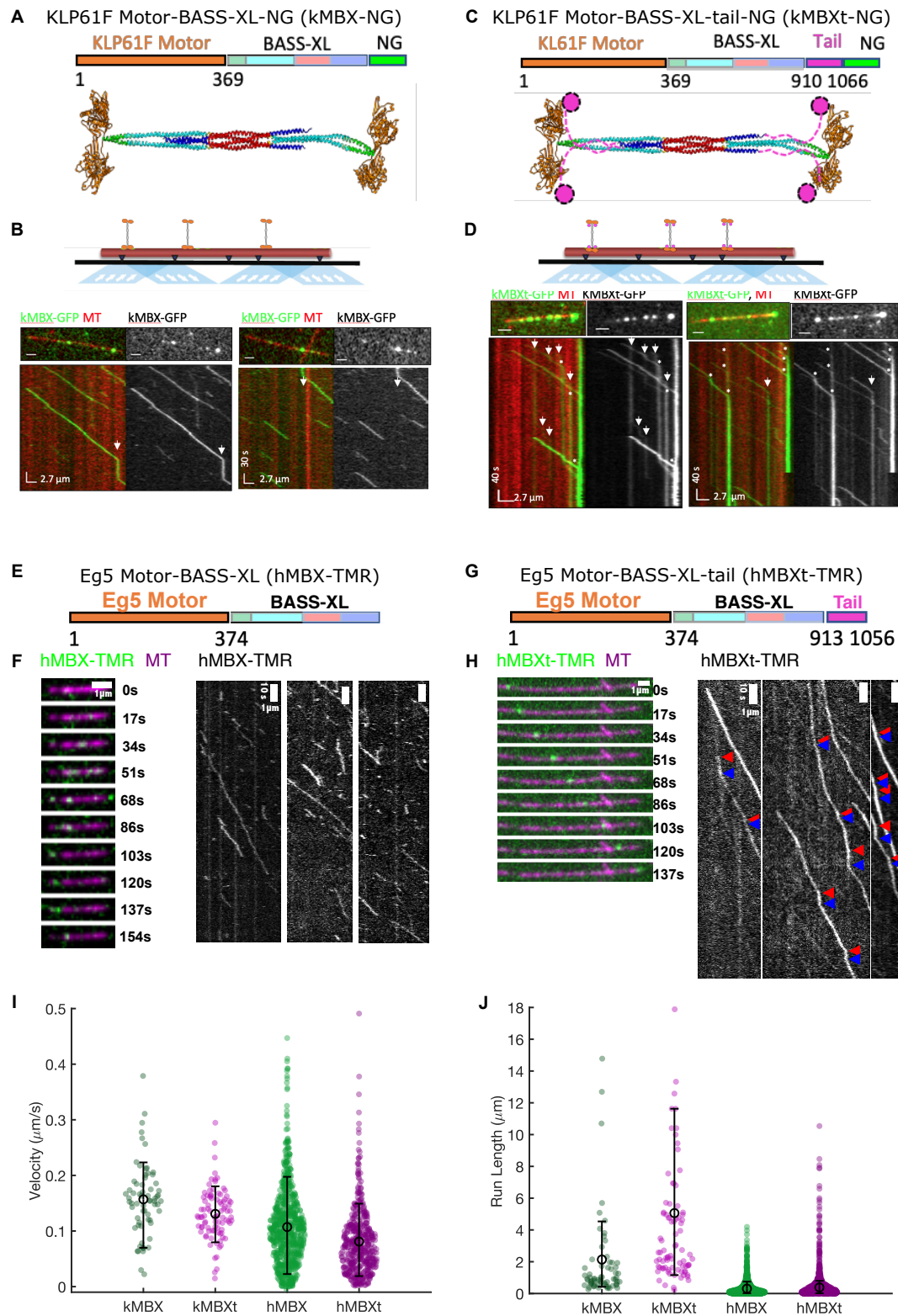
1358 Weinger, J.S., Qiu, M., Yang, G., and Kapoor, T.M. (2011). A nonmotor microtubule binding site  
1359 in kinesin-5 is required for filament crosslinking and sliding. *Curr Biol* *21*, 154-160.

1360 Zajac, A.L., Goldman, Y.E., Holzbaur, E.L.F., and Ostap, E.M. (2013). Local Cytoskeletal and  
1361 Organelle Interactions Impact Molecular-Motor-Driven Early Endosomal Trafficking. *Current*  
1362 *Biology* *23*, 1173-1180.

1363







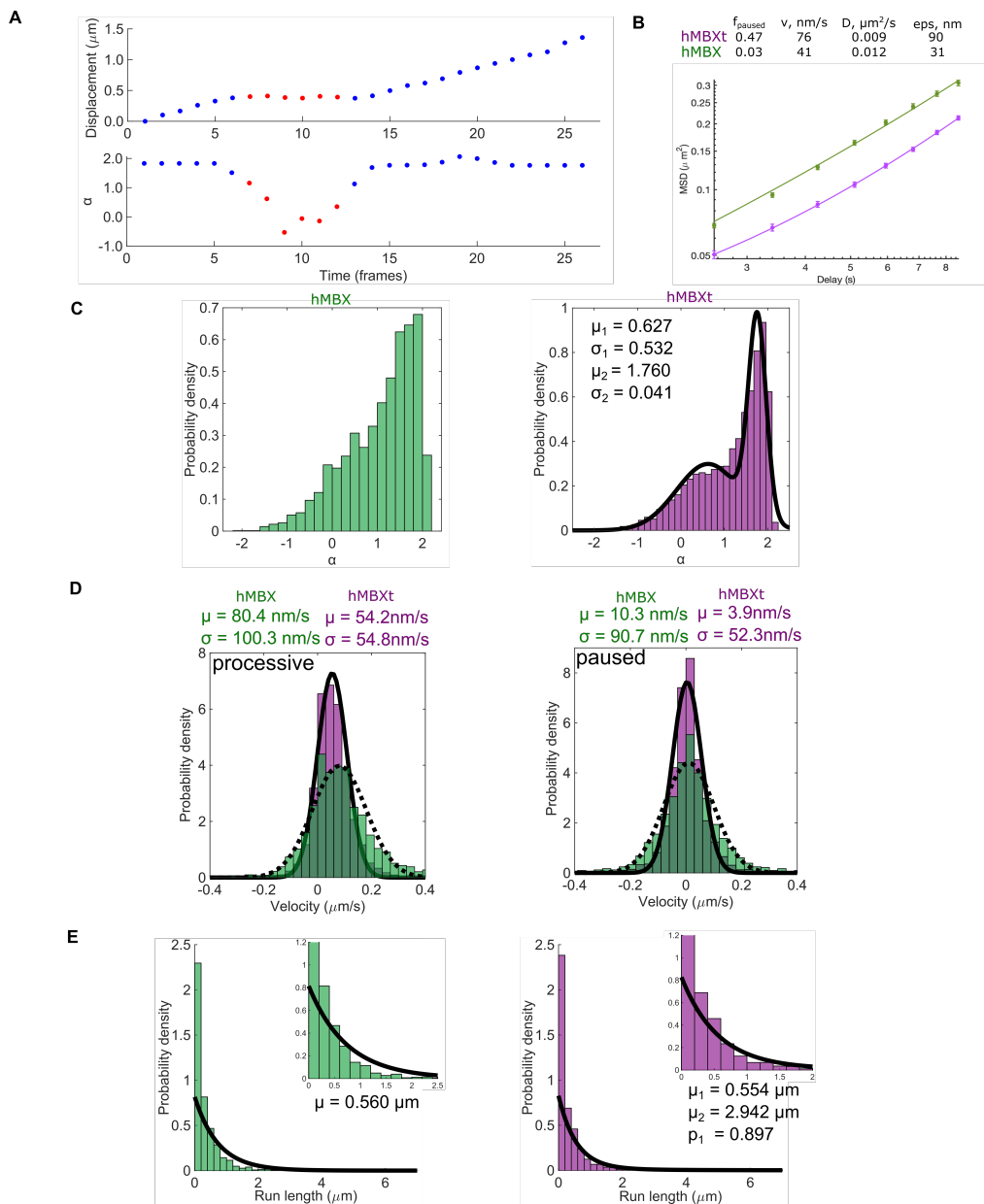


Figure 4

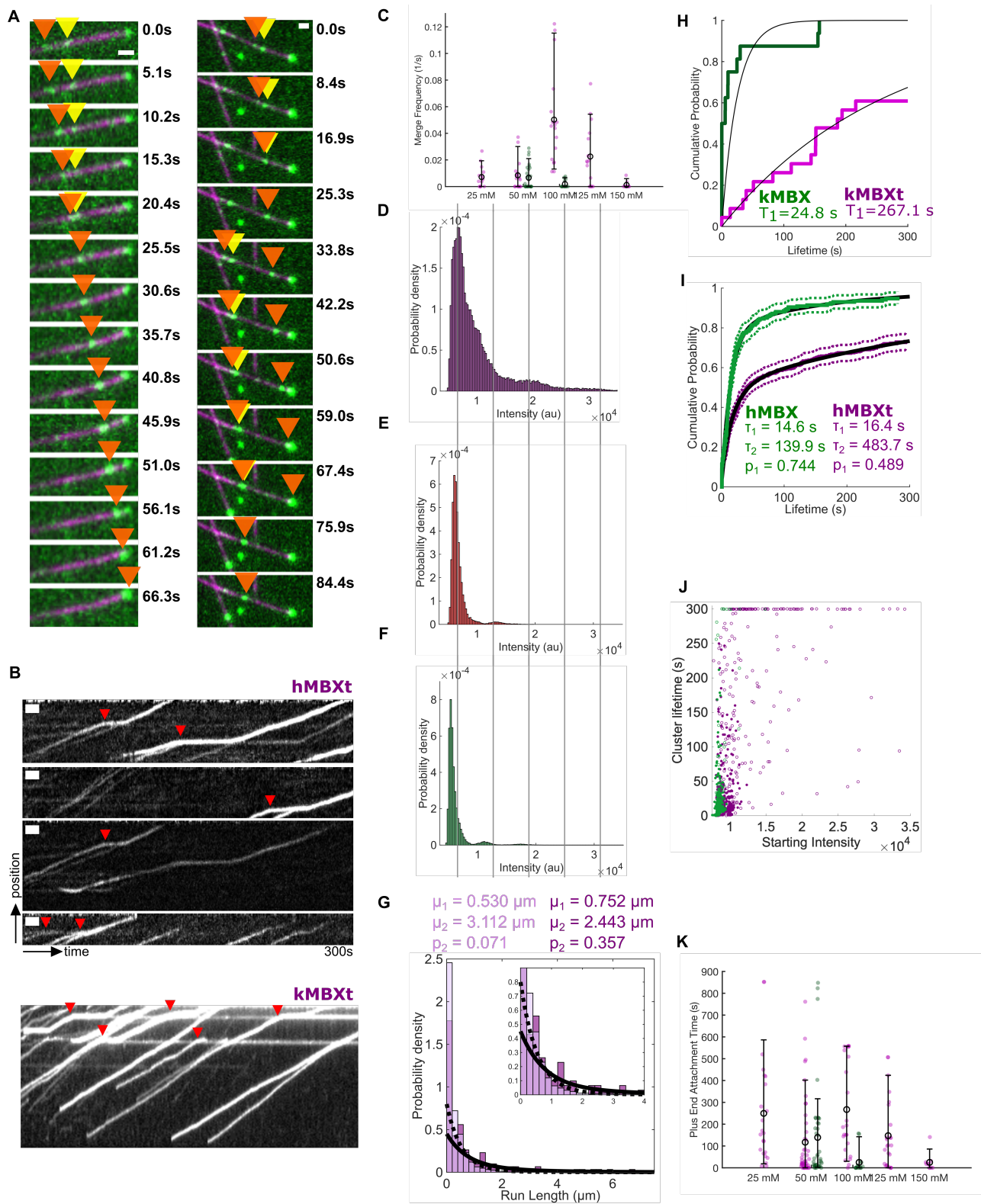


Figure 5

